

Astronomy & Astrophysics manuscript no.
(will be inserted by hand later)

Evolution of Planetary Nebulae I. An improved synthetic model

P. Marigo^{1,2}, L. Girardi^{1,2}, M.A.T. Groenewegen^{3,1}, and A. Weiss¹

¹ Max-Planck-Institut für Astrophysik, Karl-Schwarzschild-Str. 1, D-85741 Garching bei München, Germany

² Dipartimento di Astronomia, Università di Padova, Vicolo dell’Osservatorio 2, I-35122 Padova, Italy

³ European Southern Observatory, Karl-Schwarzschild-Str. 2, D-85740 Garching bei München, Germany

To appear in A&A

Abstract. We present a new synthetic model to follow the evolution of a planetary nebula (PN) and its central star, starting from the onset of AGB phase up to the white dwarf cooling sequence. The model suitably combines various analytical prescriptions to account for different (but inter-related) aspects of planetary nebulae, such as: the dynamical evolution of the primary shell and surrounding ejecta, the photoionisation of H and He by the central star, the nebular emission of a few relevant optical lines (e.g. H β ; He II λ 4686; [O III] λ 5007). Particular effort has been put into the analytical description of dynamical effects such as the three-winds interaction and the shell thickening due to ionisation (i.e. the thin-shell approximation is relaxed), that are nowadays considered important aspects of the PN evolution. Predictions of the synthetic model are tested by comparison with both findings of hydrodynamical calculations, and observations of Galactic PNe. The sensitiveness of the results to the models parameters (e.g. transition time, mass of the central star, H-/He-burning tracks, etc.) is also discussed. We briefly illustrate the systematic differences that are expected in the luminosities and lifetimes of PNe with either H- or He-burning central stars, which result in different “detection probabilities” across the H-R diagram, in both H β and [O III] λ 5007 lines. Adopting reasonable values of the model parameters, we are able to reproduce, in a satisfactory way, many general properties of PNe, like the ionised mass–nebular radius relationship, the trends of a few main nebular line ratios, and the observed ranges of nebular shell thicknesses, electron densities, and expansion velocities. The models naturally predict also the possible transitions from optically-thick to optically-thin configurations (and vice versa). In this context, our analysis indicates that the condition of optical thinness to the H continuum plays an important role in producing the observed “Zanstra discrepancy” between the temperatures determined from H or He II lines, as well as it affects the mass-increasing part of the ionised mass-radius relation. These predictions are supported by observational indications by Méndez et al. (1992). Another interesting result is that the change of slope in the electron density–nebular radius relation at $R_{\text{ion}} \sim 0.1$ pc, pointed out by Phillips (1998), is also displayed by the models and may be interpreted as the result of the progressive convergence of the PNe to the condition of constant ionised mass. Finally we would like to remark that, thanks to its computational agility, our synthetic PN model is particularly suitable to population synthesis studies, and it represents the basic ground from which many future applications will be developed.

Key words. stars: evolution – stars: AGB and post-AGB – stars: mass-loss – planetary nebulae: general

1. Introduction

Planetary Nebulae (PN) are among the most beautiful and fascinating celestial objects. They appear when low- and intermediate-mass stars, after losing their external envelopes during the AGB phase, cross the H-R diagram on their way to the white dwarf cooling sequence. During this crossing, the central nuclei become sufficiently hot to ionise the circumstellar material previously expelled. The resulting emission nebulae may turn bright enough (spe-

cially in the [O III] lines) to emerge strikingly against the background of “normal” stars, even at relatively large distances.

The study of the spectra of PNe provide unvaluable information on the chemical enrichment of the interstellar medium from low- and intermediate-mass stars, and on the kinematics of their parent populations. In general, they offer a unique tool to test stellar evolution theory (e.g. mixing processes, stellar atmospheres, evolutionary time-scales, etc.), as well the many physical processes involved (e.g. stellar winds, gas dynamics and kinematics, photoionisation, line formation, etc.) The reader can get

an overall picture by referring to the works of Pottasch (1984), Peimbert (1990), and Kwok (2000).

Indeed, the observed properties of PNe are the result of the complex interplay between several factors, whose inter-relationship cannot be summarised in simple terms. For instance, the PN lifetime – i.e. the detectability period – crucially depends on both i) the evolutionary time-scale of the central star (the time it takes to become and remain an efficient emitter of ionising photons) and ii) the dynamical time-scale of the circumstellar ejecta (including the duration of the ejection event on the AGB tip, and the time taken by the nebula to expand away from the central star).

It is clear that the detectability of a PN requires a suitable tuning between the two time-scales. If the central star evolves too quickly the brightening of the ionised nebula would correspond to a short-lived event having a low detection probability. Conversely, if the central star evolves too slowly it would start to ionise the nebula when this has already dispersed to too large radii to be detected. It follows that only when these two time-scales are comparable, we can have a maximum probability of detecting the PN phase. As a matter of fact, neither the stellar evolutionary time-scale nor the dynamical time-scale are simple predictable functions of the involved parameters.

Though all post-AGB stellar models indicate that, in general, the evolutionary speed on the H-R diagram decreases at increasing final stellar mass, other factors play non-negligible roles (such as: past stellar history, phase of the pulse cycle marking the termination of the AGB, efficiency of the fast wind, chemical composition of the envelope; see Vassiliadis & Wood 1994; Blöcker 1995 for a detailed discussion). This complexity translates into quite large uncertainties affecting, in particular, the so-called *transition time* (that determines the onset of the photoionisation phase), and the *fading time* (that determines the end of the PN lifetime).

The dynamical time-scale of the nebula is also determined by several factors including i) the properties (mass-loss rates and terminal velocities) of both the AGB (super- and/or slow) wind and the post-AGB fast wind, ii) their dynamical interaction producing gas shocks with related heating/cooling processes, and iii) the effect due to ionisation which tends to expand and accelerate the nebula as a consequence of the increased thermal pressure.

The importance of these dynamical factors has been pointed out by several past analytical works (e.g. Kahn 1983, 1989; Volk & Kowk 1985; Kahn & Breitschwerdt 1990; Breitschwerdt & Kahn 1990), and then broadly confirmed and fully analysed by (magneto-)hydrodynamical simulations of PN evolution (e.g. Schmidt-Voigt & Köppen 1987ab; Marten & Schönberner 1991; Balick et al. 1992; Mellem & Frank 1995; Schönberner & Steffen 2000, and references therein).

If, on one hand, hydrodynamical simulations are able to solve the fine details of the nebular structure getting insight into the involved physical processes, on the other hand they are so demanding in terms of comput-

ing time that only few cases of PN evolution have so far been adequately modelled. The hydrodynamical approach does not permit a systematic study of PN properties as a function of the fundamental parameters yet, i.e. stellar mass and metallicity, transition time, properties (mass-loss rates and terminal velocity) of stellar winds, etc. As a consequence, it becomes difficult also to predict the global properties of PNe populations in different galaxy environments – e.g. how they should appear for varying histories of star formation and chemical enrichment.

These aims may be achieved, taking a reasonable computational effort, with the aid of “synthetic” models of PNe, in which the main factors determining their evolution are described by means of reasonable – and necessarily simple – approximations. Several examples of synthetic PNe models can be found in the literature, as in e.g. Kahn (1983, 1989), Kahn & West (1985), Volk & Kowk (1985), Stasińska (1989), Kahn & Breitschwerdt (1990), Breitschwerdt & Kahn (1990), Stasińska et al. (1998), Stanghellini & Renzini (2000).

However, it is worth making a due distinction within the class of synthetic models. In fact, one can opt for either i) schemes based on rather crude assumptions (e.g. constant nebular mass and/or expansion velocity) which do not attempt to predict the dynamical properties and/or the ionisation structure of PNe (e.g. Stanghellini & Renzini 2000), or ii) more detailed analytical approaches which account for an overall, even if simplified, description of PN evolution, including the dynamical one (e.g. Volk & Kowk 1985; Kahn & Breitschwerdt 1990).

As far as the dynamical aspect is concerned, a further distinction should be made. Most dynamical models for PNe (both synthetic and hydrodynamical) may be classified as either *Three-Wind Models* if they consider the possible interaction between the AGB slow wind, the AGB superwind, and the post-AGB fast wind (e.g. Schmidt-Voigt & Köppen 1987ab; Marten & Schönberner 1991), or *Two-Wind Models* if they lack of a distinguishable superwind phase (e.g. Kwok et al. 1978; Volk & Kwok 1985), whose existence has actually been supported by observational evidence (see, for instance, van Loon et al. 1998).

The present study belongs to the class of *synthetic Three-Wind models* for PNe and accounts, as far as possible, for many relevant aspects, including the dynamics of the nebula, the ionisation structure of H and He by adopting stellar fluxes from non-LTE model atmospheres, and the emission of a few recombination and forbidden lines. Of course, we cannot avoid to adopt some simplifying approximations and assumptions – like spherical symmetry, constant electron temperature. However, we will show that several tests (both theoretical and observational) support the overall performance of the model, so that it can be considered as a satisfactory tool for investigating the general properties of PNe.

The outline of the paper is as follows. The basic ingredients of the model are fully described in Sect. 2. Then, after summarising the basic assumptions of the models, in Sect. 3 we give a brief overview of the model predic-

tions. We proceed in Sect. 4 with the exploration of the predicted properties of PNe as a function of the stellar mass, and of some free model parameters (e.g. transition time, electron temperature, H-/He-burning track). To this aim, we consider several observables to be reproduced, always limiting to samples of Galactic PNe. In this way, as a first step, we limit the possible effects due to different metallicities, possibly present in PNe populations of different galaxies. Concluding remarks and future aims are expressed in Sect. 5.

2. A new synthetic model of PN evolution

2.1. The general scheme

Before proceeding with the detailed description of the model, it is convenient to sketch the general scheme of the several different processes here considered.

- We start with detailed synthetic models of AGB stars of varying initial mass and metallicity. According to the adopted prescription, mass loss gets more and more efficient as the star climbs the AGB, so that most of the stellar envelope is ejected during the last “superwind” stages. We attribute proper expulsion velocities to the AGB ejecta, and follow their expansion during all the subsequent evolution.
- The central star, peeled off of its envelope, is assumed to evolve along the post-AGB track determined by its mass and initial metallicity. The so-called “transition time”, corresponding to the very initial post-AGB evolution, is left as a free parameter. At each time step, we compute the “fast wind” (momentum and kinetic energy) emitted by the central star, as well as the flux of ionising photons.
- The fast wind shapes a shell nebula through its interaction with the slower stellar wind emitted during the AGB evolution. We compute the resulting dynamical evolution by means of the so-called “interacting-winds model”. As the shell expands, it continuously accretes matter from the circumstellar layers, ejected at earlier ages and with lower velocities during the AGB phase.
- As soon as the flux of ionising photons becomes large enough (due to heating of the central star), an ionisation front proceeds through the nebula. We follow its position as a function of time, as well as the total emitted fluxes in a few relevant recombination and forbidden lines.
- The additional pressure provided by ionisation produces a thickening of the shell, that we follow in an approximative way.
- Eventually, the nebula expands to very low densities, and the central star fades along its white-dwarf cooling sequence, causing both dispersion and dimming of the emission nebula. We follow the evolution of all nebular quantities up to sufficiently large times.

The subsections below will illustrate in detail all the prescriptions we have adopted.

2.2. The AGB phase

The AGB phase is described by detailed synthetic models, covering the evolution of low- and intermediate-mass stars from the first thermal pulse up to the complete ejection of the envelope (details can be found in Marigo 1998, 2001; Marigo et al. 1996, 1998, 1999).

From these models we derive the mass of the central star as a function of the initial mass and metallicity of the progenitor, the mean radial gradient in density and chemical composition of the ejected material as a function of time (assuming spherical symmetry and stationary wind flows). A simple attempt to account for possible dynamical interaction of AGB shells ejected at different epochs with different velocities is presented in Sect. 2.4.3.

Mass-loss on the AGB is included according to the semi-empirical formalism developed by Vassiliadis & Wood (1993; hereinafter also VW93), which combines observations of variable AGB stars (Mira and OH/IR stars) with standard predictions of pulsation theory.

In brief, mass-loss during the AGB consists of two phases. Initially, for $P < 500$ days, the mass-loss rate exponentially increases with the pulsation period P

$$\log \dot{M} = -11.4 + 0.0123 P \quad (1)$$

until when, for longer periods, it attains and maintains nearly constant values, typical of the super-wind regime

$$\dot{M} = 6.07023 \times 10^{-3} \beta \frac{L}{c V_{\text{AGB}}}. \quad (2)$$

where $\beta = 1.13 (Z/0.008)$ following Bressan et al. (1998). Equation (2) is derived simply assuming that all the momentum carried by the stellar radiation field is transferred to the outer gas, and allowing the possibility for multiple scattering of photons ($\beta \geq 1$; typically $\beta \sim 2$ for solar metallicity).

In Eqs. (1) and (2), \dot{M} is given in units of $M_{\odot} \text{ yr}^{-1}$, the stellar luminosity L is expressed in L_{\odot} , the pulsation period P in days, the light speed c and the terminal velocity of the stellar wind V_{AGB} are given in km s^{-1} .

The pulsation period P is derived from the period-mass-radius relation (equation 4 in VW93), with the assumption that variable AGB stars are pulsating in the fundamental mode (see Wood et al. 1999):

$$\log P = -2.07 + 1.94 \log R - 0.9 \log M \quad (3)$$

where the period P is given in days; the stellar radius R and mass M are expressed in solar units. The wind expansion velocity V_{AGB} (in km s^{-1}) is calculated as a function of the pulsation period P (in days):

$$V_{\text{AGB}} = -13.5 + 0.056 P. \quad (4)$$

In VW93 the allowed variability range was constrained according to observations of Mira and OH/IR stars. Specifically, lower and upper limits of $V_{\text{AGB}}^{\text{min}} = 3 \text{ km s}^{-1}$ and $V_{\text{AGB}}^{\text{max}} = 15 \text{ km s}^{-1}$, respectively, were adopted.

At this point it should be remarked that, for our purposes, $V_{\text{AGB}}^{\text{max}}$ is a quite crucial quantity, since it essentially

determines the characteristic velocity of the superwind ejecta, from which most PNe are thought to originate. Therefore, setting $V_{\text{AGB}}^{\text{max}}$ is practically equivalent to specify the expansion velocity of the main ejection event at the end of the AGB phase, which is clearly of great relevance to the subsequent dynamical evolution of the PN. A few alternative prescriptions for $V_{\text{AGB}}^{\text{max}}$ are presented below.

2.2.1. The maximum velocity

Several factors affect the terminal velocity of the AGB wind. Observations of OH/IR and Mira variable stars indicate that V_{AGB} may range over a relatively large range, i.e. from ~ 8 to 30 km s^{-1} , with a typical mean value of $\sim 14 - 15 \text{ km s}^{-1}$ for galactic variables (e.g. Gussie & Taylor 1994; Groenewegen & de Jong 1998; Groenewegen et al. 1998, 1999; van Loon 2000), and possibly lower for variables belonging to more metal poor galaxies (e.g. $V_{\text{AGB}}(\text{LMC})/V_{\text{AGB}}(\text{Galaxy}) \sim 0.5 - 0.6$ for OH/IR stars, as pointed out by Wood et al. 1992). In the framework of radiation-driven dusty winds, this fact would be the result of lower dust-to-gas ratio, δ , at decreasing metallicity (e.g. $V_{\text{AGB}} \propto \delta^{0.5}$ according to the theoretical expectations of Habing et al. 1994). Moreover, both observations (e.g. Loup et al. 1993) and model predictions (e.g. Netzer & Elitzur 1993) converge to the result that V_{AGB} is larger for carbon-rich stars than for oxygen-rich stars, owing to the different absorption properties of chemically different dust grains.

In addition to a dependence on chemical composition, calculations of radiative transfer in dust-driven winds (e.g. Netzer & Elitzur 1993; Habing et al. 1994; Krüger et al. 1994; Ivezić & Elitzur 1995) have pointed out that the terminal velocity is affected by several other factors, i.e. mass-loss rate, radius of dust grain, and stellar luminosity.

A theoretical finding, which is relevant to the present analysis, is that at sufficiently high mass-loss rates ($\dot{M} \gtrsim 10^{-6} M_{\odot}$), the terminal velocity is expected to be practically independent from \dot{M} (Habing et al. 1994).

On the basis of all these aforementioned elements (both theoretical and observational), let us now consider some prescriptions we may reasonably adopt for $V_{\text{AGB}}^{\text{max}}$, namely:

1. $V_{\text{AGB}}^{\text{max}} = \text{constant}$, say 15 km s^{-1} , regardless of any other parameter. This is the simplest possible assumption, and is made for instance, by VW93 and Marigo et al. (1996, 1998).

2. $V_{\text{AGB}}^{\text{max}} = f(Z) = 6.5(Z/0.008) + 0.00226 P$, (5) which includes a metallicity dependence, according to an empirical calibration based on OH/IR variables of the Galaxy and LMC (Bressan et al. 1998). Such a prescription has been employed in the AGB synthetic calculations adopted here (Marigo et al. 1999; Marigo 2001). For typical values of $P > 500 - 2000$ days, we get $V_{\text{AGB}}^{\text{max}} \sim 8 - 11 \text{ km s}^{-1}$ for $Z = 0.008$, and $V_{\text{AGB}}^{\text{max}} \sim 17 - 20 \text{ km s}^{-1}$ for $Z = 0.02$. We note that, at fixed

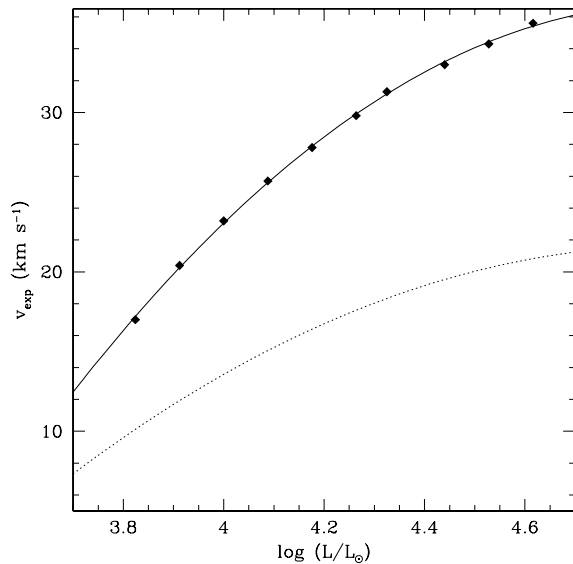


Fig. 1. Expected dependence of V_{AGB} on stellar luminosity, according to Krüger et al. 1994 (squares). The parabolic fitting relation (Eq. 6) is shown (solid line), together with that obtained scaling it by a factor $f_v = 0.588$ (dotted line). See Sect. 2.2.1 for explanation

metallicity, $V_{\text{AGB}}^{\text{max}}$ is almost constant, due to the weak dependence on the pulsation period.

3. $V_{\text{AGB}}^{\text{max}} = f(L) = A(\log L)^2 + B \log L + C$, (6) which includes a luminosity dependence, according to the results of two-fluid-model calculations for dust-driven winds (Krüger et al. 1994). The fitting coefficients (to reproduce their figure 12, see also Fig. 1) are $A = -16.7282$, $B = 164.1858$, and $C = -366.0314$. Of course, these numbers only apply to a specific set of calculations performed by Krüger et al. (1994). Therefore, in order to specify $V_{\text{AGB}}^{\text{max}}$ in our model, it may be reasonable to keep the relative trend with the stellar luminosity as predicted by Krüger et al., and scale it by a proper multiplicative factor, f_v , calibrated on some suitable constraint (Sect. 4.1).

2.3. The post-AGB evolution of the central star

The post-AGB tracks are taken from Vassiliadis & Wood (1994) data set, that spans a large range of core masses ($\sim 0.55 M_{\odot} - 0.95 M_{\odot}$) and metallicities ($Z = 0.016, 0.008, 0.004$, and 0.001). They also include both H- and He-burning central stars, i.e. stars that have left the AGB at different phases of their thermal pulse cycles, while they were efficiently burning their nuclear fuel either in the H- or in the He-burning shell. These two situations lead to very different lifetimes during the post-AGB, including the possible presence of a late flash and “final loop” for He-burners. All evolutionary tracks start at $\log T_{\text{eff}} = 4$ which, in the case of He-burning stars, marks the point in the blue-ward part of the last loop in the H-R diagram.

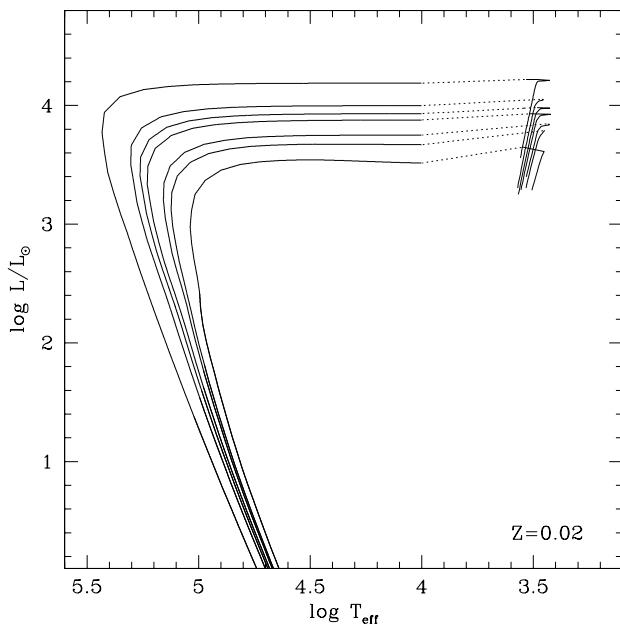


Fig. 2. Evolutionary tracks in the H-R diagram from the first thermal pulse on the AGB to the cooling sequences of White Dwarfs. The transition from the tip of synthetic AGB models to the starting point of the post-AGB H-burning tracks of the same core mass is shown (dotted line)

For all the details about the models the reader should refer to the Vassiliadis & Wood (1994) paper.

At fixed metallicity, the match between the adopted AGB synthetic models and the post-AGB tracks is performed by interpolating the latter data as a function of the stellar mass left at the end of the AGB. An example is illustrated in Fig. 2.

Minor differences between the stellar luminosity at the tip of the AGB and that of the horizontal part of the post-AGB track in the H-R diagram reflect small differences between the core mass-luminosity relation derived by Vassiliadis & Wood (1993, 1994), and that adopted in the synthetic AGB models here in use (Wagenhuber & Groenewegen 1998).

As we can see, the early post-AGB stages (i.e. after the star has left the AGB up to $\log T_{\text{eff}} = 4$) are not covered by the tracks (dotted line in Fig. 2). They correspond to the transition from the end of the AGB to the starting of the ionisation phase, i.e. the period in which the central star does not emit enough UV photons to ionise the H atoms in the surrounding nebula. Large uncertainties affect the duration of such phase – the so-called *transition time*, t_{tr} (see Renzini 1989; Schönberner 1990) – essentially due to our poor knowledge of the properties of the stellar wind, as it evolves from the super-wind regime to the fast-wind regime (see Blöcker 1995 for an analysis of this point).

Moreover, even for a given prescription for mass-loss, Vassiliadis & Wood (1994) find no evident correlation between t_{tr} and the mass of the central star, but rather a

dependence on the phase of the pulse cycle at which the star leaves the AGB (Vassiliadis & Wood 1994). For all these reasons, we choose to adopt t_{tr} as a free parameter in our model, comprised in the range 500 yr – 10 000 yr.

2.3.1. The fast wind

Mass-loss during the post-AGB phase of the central star is a crucial process as it affects the evolutionary time-scales and hence observable properties of PNe.

In this model, we describe the fast wind adopting the prescriptions from Vassiliadis & Wood (1994). This formalism combines the results of the radiation-pressure-driven-wind theory for hot stars (Pauldrach et al. 1988), with empirical correlations observed for both AGB stars and central stars of planetary nebulae. In this way, a continuous change of the wind parameters is allowed, as the evolution proceeds from the super-wind regime, typical of the last stages of the AGB phase, to the accelerating fast wind regime during the post-AGB phase.

Let us summarise the basic prescriptions. The terminal wind velocity, v , of the fast wind is calculated with

$$\log \frac{v}{v_{\text{esc}}} = -2.0 + 0.52 \log T_{\text{eff}}, \quad (7)$$

where the escape velocity is

$$v_{\text{esc}} = \left[(1 - \Gamma) \frac{2GM}{R} \right]^{1/2}, \quad (8)$$

and Γ is the ratio of the stellar to the Eddington luminosity. This latter is given by

$$L_{\text{Edd}} = \frac{0.2(1+X)}{4\pi c GM} \quad (9)$$

where the other symbols have the usual meaning. Equation (7) is a linear fit to observed data, including central stars of PNe, B stars, A-F supergiants, and a fiducial point for OH/IR stars.

Let us denote by \dot{M}_{lim} the radiation-pressure-driven mass-loss limit, corresponding to the case in which all the momentum carried by the radiation field is transferred to the wind gas:

$$\dot{M}_{\text{lim}} = \frac{L}{cv} \quad (10)$$

Then, the mass-loss rate, \dot{M} , in the PN phase is calculated assuming a linear relation between $\log \dot{M}/\dot{M}_{\text{lim}}$ and $\log T_{\text{eff}}$:

$$\log \frac{\dot{M}}{\dot{M}_{\text{lim}}} = -3.92 + 0.67 \log T_{\text{eff}} \quad (11)$$

as derived by Vassiliadis & Wood (1994) following the theoretical results by Pauldrach et al. (1988).

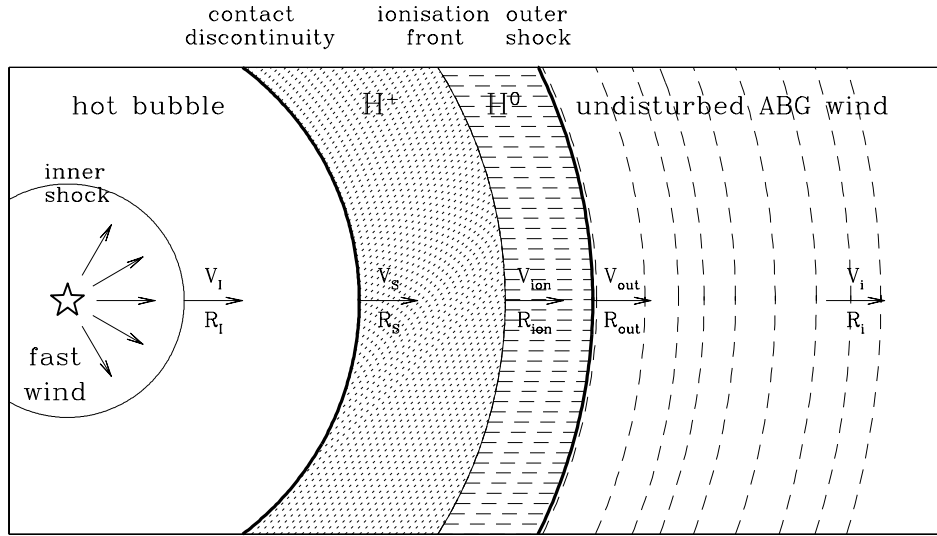


Fig. 3. Schematic sketch of the system composed by the central star, shocked PN shell, and undisturbed AGB wind

2.4. The dynamical evolution of the shocked nebula

The dynamical evolution of planetary nebulae is followed in the framework of the interacting-winds model, first developed by Kwok et al. (1978), Kwok (1983), Kahn (1983), and substantially improved by Volk & Kwok (1985, hereinafter also VK85). Major improvements to the VK85 scheme are included, by combining complementary prescriptions from other studies (i.e. Kahn 1983; Kahn & Breitschwerdt 1990; Breitschwerdt & Kahn 1990), as described in the next sections.

For the sake of clarity, only the basic concepts and definitions are briefly recalled in the following (see also Table 1). For more details the reader should refer to the aforementioned papers.

The dynamical evolution of PNe is considered the result of the interaction between the fast wind emitted by the central star during the post-AGB evolution, and the slow circumstellar wind previously ejected during the AGB phase. When the fast-moving gas catches up with the slower one, a dense shell forms and two shock waves are generated. The inner shock is located at the point where the fast wind encounters the slow-moving gas. The outer shock is at the outer boundary of the shell, beyond which the undisturbed AGB wind is expanding outward. Depending on the efficiency of radiative cooling, the hot shocked gas from the fast wind may fill (or not) the bubble extending from the inner shock up to the so-called contact discontinuity, i.e. the inner rim of the shell. No heat or gas is assumed to pass across it. The shocked shell may be partially or totally ionised by the UV photons emitted by the central star.

According to the dominant mechanism causing the expansion of the shell, we can distinguish two dynamical phases, namely: the initial *momentum-driven phase* and the subsequent *energy-driven phase*.

Table 1. Adopted notation for relevant quantities

\dot{M}_{AGB}	mass-loss rate during the AGB phase
\dot{m}	mass-loss rate during the post-AGB phase
M_S	mass of the shell
R_I	radius of the inner shock
R_S	radius of the contact discontinuity (thin-shell)
R_S^*	radius of the contact discontinuity (thick-shell)
R_{ion}	radius of the ionisation front (thick-shell)
R_{out}	radius of the outer shock
V_{AGB}	terminal velocity of the AGB wind
v	terminal velocity of the fast wind
V_I	velocity of the inner shock front
V_S	expansion velocity of the shell (thin-shell)
V_S^*	velocity related to R_S^* (thick-shell)
V_{ion}	velocity of the ionisation front (thick-shell)
P	pressure of the hot shocked gas

Hereinafter we convene to set the evolutionary time equal to zero ($t = 0$) at the end of the AGB phase, i.e. at the onset of the momentum-driven phase.

2.4.1. The momentum-driven phase

During the initial stages after the end of the AGB phase, the rate of radiative cooling is larger than the rate of kinetic input from the fast wind ($\dot{m}v^2/2$), so that the inner shock can be considered isothermal. The shocked matter can be compressed effectively and the inner front is pushed quite close to the contact discontinuity ($R_I \approx R_S$), as it turns out from hydrodynamical calculations (e.g. Marten & Schönberner 1991). Under these conditions, the driving force which makes the shocked shell move outward is the transfer of momentum from the fast wind. In our model, we account for this phase by adopting the prescriptions presented in Kahn & Breitschwerdt (1990, hereinafter also KB90).

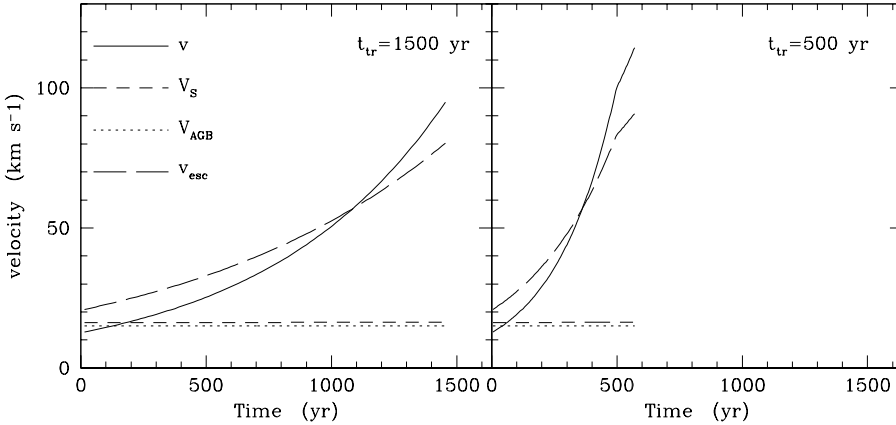


Fig. 4. Relevant velocities during the momentum-driven phase of the expanding shell surrounding a central star with mass $0.6 M_{\odot}$ and initial solar composition, for two choices of the transition time as indicated left panel: model 1, right panel: model 5; see Table 2. Time is set to zero at the end of the AGB phase

From the conditions of mass and momentum conservation applied to the system composed by the fast wind and the swept shell, one gets simple relations expressing the time evolution of the shell mass

$$\frac{dM_S}{dt} = \dot{M}_{\text{AGB}}(t) \left[\frac{V_S(t)}{V_{\text{AGB}}(t)} - 1 \right], \quad (12)$$

and the radius of the contact discontinuity

$$\frac{dR_S}{dt} = V_S(t) = \left[1 + \sqrt{\alpha(t)} \right] V_{\text{AGB}}(t), \quad (13)$$

where α is defined according to:

$$\dot{m}(t)v(t) = \alpha(t)\dot{M}_{\text{AGB}}(t)V_{\text{AGB}}(t) \quad (14)$$

For typical values of the winds parameters involved (e.g. $\dot{M}_{\text{AGB}} \sim 10^{-4} - 10^{-5} M_{\odot} \text{ yr}^{-1}$, $V_{\text{AGB}} \sim 10 - 20 \text{ km s}^{-1}$, $\dot{m} \sim 10^{-7} - 10^{-8} M_{\odot} \text{ yr}^{-1}$, $v \sim 100 - 1000 \text{ km s}^{-1}$) the quantity α is found to be less than unity ($\sim 0.01 - 0.1$). This means that the rate of momentum injection to the gas from the accelerating fast wind is lower than that due to the AGB superwind, i.e. $\dot{m}v < \dot{M}_{\text{AGB}}V_{\text{AGB}}$.

Under the condition of a steady rate of momentum injection, i.e. if $\alpha = \text{const.}$, the shell's motion would be uniform, as assumed by KB90. Here we consider the general case that α depends on time – since all the quantities in Eq. (14) depend on time –, but find that α increases just negligibly in our models, thus recovering the KB90 assumption that the velocity of the shell is almost constant during the momentum-driven phase. An example is shown in Fig. 4 where $V_{\text{AGB}} = 15.0 \text{ km s}^{-1}$ and $V_S \sim 16.3 \text{ km s}^{-1}$, in very good agreement with the results of hydrodynamical calculations by Kifonidis (1996). The plot also shows the predicted speed-up of the fast wind (with velocity v according to the prescriptions in Sect. 2.3.1) and the escape velocity v_{esc} during the momentum driven phase.

The momentum-driven phase ends when the hot shocked gas is able to fill the interior in a time shorter than the cooling time. Following KB90, the change-over time t_* from the momentum-driven phase to the energy-driven phase, crucially depends on the velocity v of the fast wind:

$$t_* = 5.23 \frac{\dot{M}_{\text{AGB}} q \alpha}{(1 + \sqrt{\alpha}) v^6} \quad (15)$$

where $q = 4 \times 10^{32} \text{ cm}^6 \text{ g}^{-1} \text{ s}^{-4}$ (Kahn 1976) and all other quantities are in c.g.s. units. We obtain that Eq. (15) is fulfilled typically for $v \sim 100 - 150 \text{ km s}^{-1}$, in agreement with the findings of KB90. Clearly, t_* is quite sensitive to the evolutionary speed of the central star during the initial post-AGB stages, as illustrated in Fig. 4 for two choices of the transition time.

Finally, it is worth remarking that in all our models, during the momentum-driven phase, the shell remains essentially neutral, the ionisation of H possibly starting towards the end of this phase and involving an almost negligible part of the nebula.

2.4.2. The energy-driven phase

The dynamical evolution of the shell at $t > t_*$ is mainly controlled by the kinetic energy input from the fast wind, which can be substantially thermalised as radiative cooling is inefficient. A hot bubble develops, and the physical conditions of the interior gas are those produced by a strong adiabatic shock. The front of the inner shock sits very close to the central star (i.e. $R_I \ll R_S$). During this phase the thermal pressure inside the hot bubble is the driving force acting on the shell.

In our model, as soon as $t = t_*$ we switch to the dynamical description developed by VK85. From the conditions of conservation of mass, momentum, and energy applied to the system consisting of the hot bubble and the shell, one finally ends up with a set of coupled, non-linear, first-order differential equations:

$$\frac{dR_S}{dt} = V_S \quad (16)$$

$$\frac{dM_S}{dt} = \dot{M}_{\text{AGB}} \left(\frac{V_S}{V_{\text{AGB}}} - 1 \right) \quad (17)$$

$$\frac{dV_S}{dt} = \frac{1}{M_S} \left[4\pi R_S^2 P - \dot{M}_{\text{AGB}} \frac{(V_S - V_{\text{AGB}})^2}{V_{\text{AGB}}} \right] \quad (18)$$

$$\frac{dP}{dt} = \frac{(1/2)\dot{m}v^2 - 10\pi P_S V_S R_S^2 + 6\pi P_S V_I R_I^2}{2\pi(R_S^3 - R_I^3)} \quad (19)$$

Radiative cooling in the shocked region is neglected, which is a reasonable approximation during the energy-driven phase. The numerical integration of Eqs. (16) – (19) is

performed explicitly, with a integration step much shorter (i.e. 1/100) than the actual evolutionary time step. This latter is chosen so that the maximum variation either in the effective temperature or in the luminosity of the central stars cannot be larger than 0.01 dex. The initial conditions for integration are determined by the values of the variables at the end of the momentum-driven phase.

It is worth remarking that in our model, both \dot{M}_{AGB} and V_{AGB} are not constant as assumed in many past works, but are given as a function of time according to the synthetic calculations of the AGB phase (see Sect. 2.2). This means that, at each instant, \dot{M}_{AGB} and V_{AGB} represent the mass-loss rate and the expansion velocity of the wind layer previously ejected during the AGB, which is now being swept by the shocked shell.

In Eq. (19) the radius (R_I) and velocity (V_I) of the inner shock also enter. It was shown by hydrodynamical calculations (e.g. Marten & Schönberner 1991) that R_I rapidly decreases from its initial value ($\sim R_S$, as in the momentum-driven phase) to a value small compared to R_S . Therefore, it is reasonable to adopt for R_I at each time step the asymptotic solution as derived by VK85:

$$\frac{R_I}{R_S} \approx \sqrt{\frac{3\dot{m}v}{4\dot{M}_{\text{AGB}}V_{\text{AGB}}}} \left(\frac{V_S}{V_{\text{AGB}}} - 1 \right)^{-1} \quad (20)$$

At each instant, the velocity $V_I = dR_I/dt$, is derived from Eq. (20).

2.4.3. Dynamical interaction of AGB shells

As pointed out by hydrodynamical simulations (e.g. Frank et al. 1990, 1994; Steffen & Schönberner 2000; Corradi et al. 2000), beyond the primary shocked shell blown by the fast wind, dynamical interactions also occur in the “undisturbed” AGB wind, which may account for a number of complex morphological and emission features, i.e. crowns, edges, multiple shells, extended halos, etc. It is obvious that a similar detailed analysis is out of reach for our analytical model, nevertheless we can at least attempt to give a zero-order description of AGB wind interactions.

According to the adopted formalism for the AGB wind (VW93), both \dot{M} and V_{AGB} increase with time until the natural onset of the superwind regime. In this scenario, it turns out that interactions between TP-AGB ejecta with different expansion velocities may be possible, even if they are not yet reached by the outer shock front produced by the fast wind.

Let us consider three consecutive AGB shells, with masses M_1 , M_2 , M_3 , that are expanding with constant radial velocities at a given instant t . For the sake of simplicity, we denote with $(V_i; i = 1, 4)$ the velocities at the shell boundaries of radii $(R_i; i = 1, 4)$, so that the i^{th} -shell is moving with velocity V_i . The situation is sketched in Fig. 5. Suppose also that $V_2 > V_3$. As a consequence, it may happen that at a certain time $t + dt$ during the expansion, shell 2 catches up shell 3. This would cause a sort of overlap of gas shells with different dynamical properties,

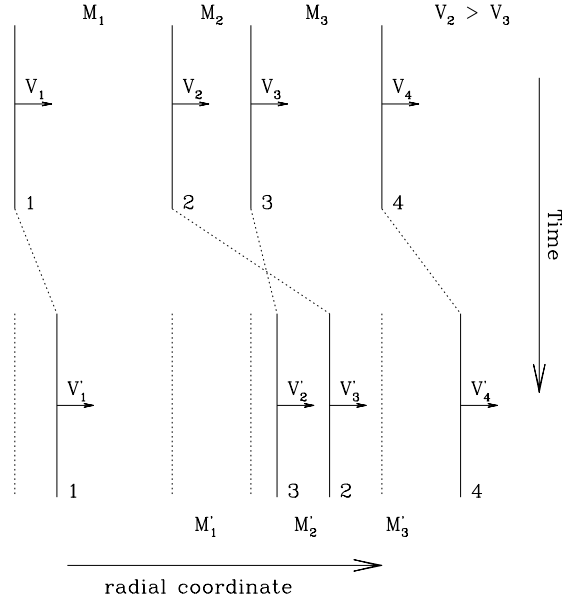


Fig. 5. Schematic representation of the possible interaction between expanding shells ejected during the AGB. See text for a complete description

and hence a change in the mass and velocity distributions along the radial coordinate.

To describe the final result (at time $t + dt$) of this interaction we adopt the following simple scheme. We denote with

$$\begin{cases} R'_1 = R_1 + V_1 dt \\ R'_2 = R_3 + V_3 dt \\ R'_3 = R_2 + V_2 dt \\ R'_4 = R_4 + V_4 dt \end{cases} \quad (21)$$

the new radial location of the shell boundaries (at increasing distance; note the exchange between indices 2 and 3), and assume that $V'_1 = V_1$ and $V'_4 = V_4$ (i.e. at these radii the expansion motion is undisturbed). Then, the problem is to determine the five unknowns (M'_1 , M'_2 , M'_3 , V'_2 , and V'_3) which characterise at time $t + dt$ the shells delimited by radii R'_j , as given by Eqs. (21). From imposing the mass conservation of the system composed by the three original shells, we get the new masses:

$$\begin{cases} M'_1 = M_1 - \Delta M_1 \\ M'_2 = M_2 + \Delta M_1 + \Delta M_2 \\ M'_3 = M_3 - \Delta M_3 \end{cases} \quad (22)$$

where

$$\Delta M_1 = \frac{R'_2{}^3 - R'_3{}^3}{R'_2{}^3 - R'_1{}^3} M_1 \quad (23)$$

$$\Delta M_2 = \frac{R'_2{}^3 - R'_3{}^3}{R'_4{}^3 - R'_3{}^3} M_3,$$

whereas from the conditions of momentum and energy conservation:

$$M_1 V_1 + M_2 V_2 + M_3 V_3 = M'_1 V'_1 + M'_2 V'_2 + M'_3 V'_3 \quad (24)$$

$$M_1 V_1^2 + M_2 V_2^2 + M_3 V_3^2 = M'_1 V'_1{}^2 + M'_2 V'_2{}^2 + M'_3 V'_3{}^2$$

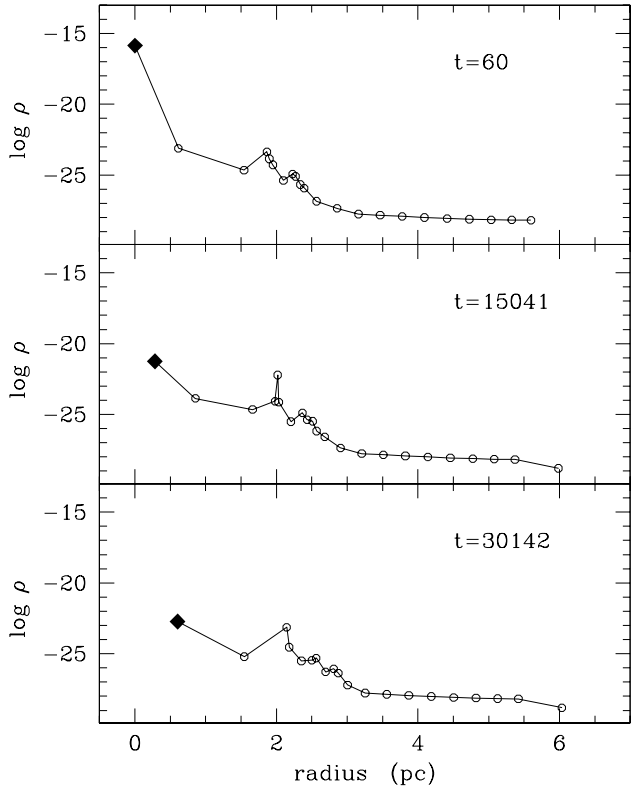


Fig. 6. Evolution of the radial density (in gr cm^{-3}) structure of the circumstellar ejecta (model 4; see Table 2) at selected ages (indicated in yr) during the post-AGB phase. $t = 0$ would correspond to the moment in which the central star leaves the AGB. In each panel, filled squares mark the average density in the primary shocked shell, whereas open circles correspond to the sequence of unperturbed AGB shells

we obtain the new velocities V'_2 and V'_3 (for which we omit to present the formulas due to their trivial derivation).

This produces evident perturbations in the density pattern that would be otherwise expected for a stationary gas flow. A possible consequence of the shell overlap sketched in Fig. 5 is the appearance of a density enhancement within the new shell 2 (with mass $M_2 + \Delta M_1 + \Delta M_2$).

According to the above prescriptions we find that this kind of dynamical events begins to affect the circumstellar ejecta in the last stages of the AGB evolution (i.e. after the onset of the super-wind regime), and usually involves shells ejected during the transition from the slow AGB wind to the superwind. This feature is in agreement with the hydrodynamical findings by Steffen & Schönberner (2000).

An example is shown in Fig. 6. We can notice that non-negligible density enhancements show up in the radial density structure of the model. These density spikes are rather close to the primary shocked shell, while the long tail of slow low-density shells remains unperturbed.

We are completely aware that such approach is an extremely rough description of the real situation, which can

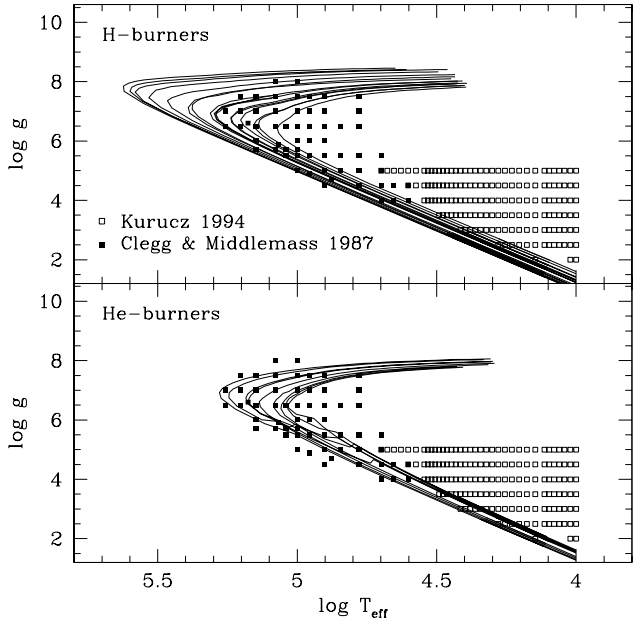


Fig. 7. Available data grid for the ionising rates of H and He^+ in the $\log T_{\text{eff}} - \log g$ plane according to model atmospheres of Clegg & Middlemass (1987; filled squares) and Kurucz (1994; empty squares). The sets of H- and He-burning post-AGB tracks from Vassiliadis & Wood (1994) are superimposed

be handled correctly only with the aid of hydrodynamics. Nevertheless, it may be interesting to get a first hint of likely interaction events (i.e. when and where they might occur) in the unperturbed AGB ejecta surrounding the primary shocked nebula. Furthermore, we remark that the dynamical scheme presented in this section does not affect any of the relevant predictions, as long as the PN is assimilated to the primary shocked shell, as in the analytical interacting-winds model (see Sect. 2.4).

2.5. Photoionisation rates for H and He^+

As the central star evolves at increasing effective temperatures along the horizontal part of the H-R track, it starts emitting UV photons that can ionise the surrounding nebula.

In this study we account for the photoionisation of H and He^+ , which occurs when a significant fraction of the emergent photons has a wavelength shorter than 911 Å (for $T_{\text{eff}} \gtrsim 30\,000$ K) and 228 Å (for $T_{\text{eff}} \gtrsim 60\,000$ K), respectively. Ionisation fluxes (in $\text{cm}^{-2} \text{s}^{-1}$) are derived from atmosphere models, namely: the LTE models calculated by Kurucz (1994) in the ranges: $10\,000 \leq T_{\text{eff}} \leq 40\,000$ K, $2.0 \leq \log g \leq 5.0$; and the non-LTE models by Clegg & Middlemass (1987) in the ranges: $40\,000 \text{ K} \leq T_{\text{eff}} \leq 180\,000$ K, $4.0 \leq \log g \leq 8.0$. In the adopted model atmospheres the abundance ratio $\text{He}/\text{H} = 0.1$ (by number) is assumed.

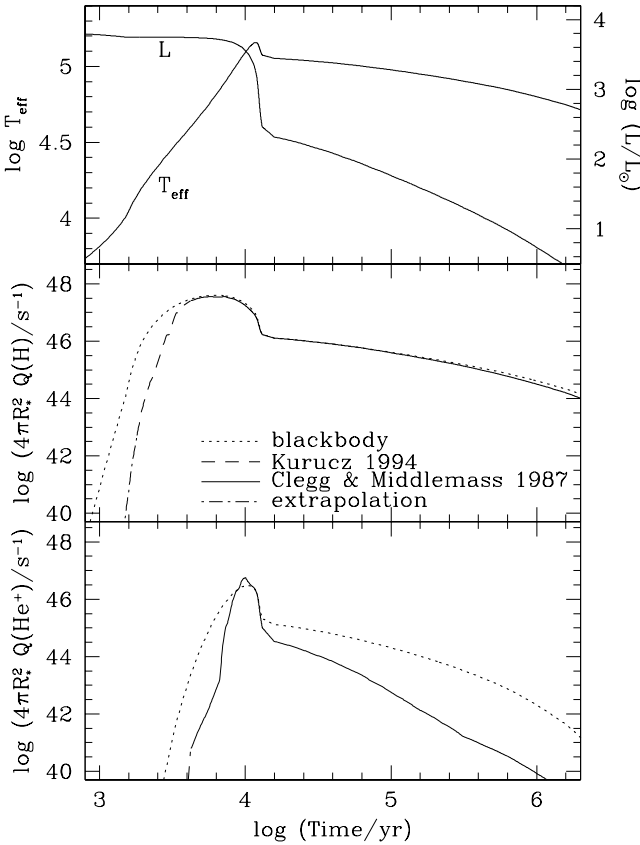


Fig. 8. Ionisation rates as a function of time for a $0.6 M_{\odot}$ post-AGB central star (model 4 in Table 2). See text for more details

In Fig. 7 the adopted grids of model atmospheres are shown in the $\log T_{\text{eff}} - \log g$ plane, together with the sets of post-AGB tracks for both H- and He-burner central stars. For each grid point, ionising fluxes are obtained integrating the synthetic spectra

$$Q = \int_{h\nu_1}^{h\nu_2} \frac{L_{\nu}}{h\nu} d(h\nu) \quad (25)$$

with $h\nu_1 = 13.6$ eV and $h\nu_2 = 54.4$ eV for the H continuum, and $h\nu_1 = 54.4$ eV and $h\nu_2 = \infty$ for the He^+ continuum, thus neglecting absorption by neutral helium in the nebula. These calculations yield $Q(\text{H}^0)$ and $Q(\text{He}^+)$ as a function of both effective temperature (in the range $T_{\text{eff}} : 10 - 180 \times 10^3$ K) and surface gravity (in the range $\log g : 2.0 - 8.0$) of the hot star.

Within the $g - T_{\text{eff}}$ range spanned by the model atmospheres, a bi-linear interpolation in $\log T_{\text{eff}}$ and $\log g$ over this data grid is then adopted to evaluate the current ionisation fluxes along the post-AGB tracks. For possible points not covered by the grid, we extrapolate the model data in $\log g$ for $T_{\text{eff}} < 180 000$ K, and we assume a blackbody spectral energy distribution for $T_{\text{eff}} > 180 000$ K (temperatures attained only by H-burning central stars with $M \gtrsim 0.7 M_{\odot}$; see Fig. 7).

An example is shown in Fig. 8, where the ionisation rates for H and He^+ (i.e. $4\pi R_*^2 Q(\text{H})$ and $4\pi R_*^2 Q(\text{He}^+)$ in

s^{-1} , where R_* is the stellar radius) are calculated as a function of time for an evolving central star with a mass of about $0.6 M_{\odot}$. Predictions from Kurucz and Clegg & Middlemass model atmospheres are compared to blackbody integrations.

The temporal behaviour of the ionisation rates is controlled by the changes in T_{eff} and L , and the evolutionary speed of the central stars. In Fig. 8 we can see that the photoionisation rates significantly increase as the star heats up at nearly constant luminosity, reach a peak (in proximity of the knee of the H-R track, at the maximum of T_{eff} in the top panel) and then quickly fall down when the luminosity drops. Subsequently, the slower decrease of the ionisation rates reflects the drastic deceleration of the evolutionary speed. We can also notice that in general $Q(\text{H}) > Q(\text{He}^+)$, and the peak duration is larger for $Q(\text{H})$ compared to $Q(\text{He}^+)$.

As far as the ionisation of H is concerned, we notice that the blackbody assumption notably overestimates the continuum flux for $T_{\text{eff}} < 40 000$ K, whereas it approximates well the atmosphere models at higher temperatures.

Much larger differences exist between the He^+ ionisation fluxes predicted according to the blackbody and stellar atmospheres models. These discrepancies are due to important non-LTE effects that significantly alter the relative number of neutral, single, and doubly ionised He expected under LTE conditions (Clegg & Middlemass 1987).

As shown in the bottom panel of Fig. 8, for most of the post-AGB evolution the adoption of a blackbody spectrum leads also to overestimate the He^+ continuum, except for the emission peak corresponding to the highest effective temperatures, before the decline of the stellar luminosity (see top panel). Such remarkable excess of UV photons may be one of the main factors at the origin of the so-called Zanstra discrepancy (refer to Gruenwald & Viegas 2000 for a recent analysis; see also Sect. 4.4).

2.6. Ionised mass

The ionisation structure of the nebula is solved with the aid of simple but reasonable prescriptions. Once the ionising rates emitted by the central star are known, the ionised mass can be singled out, provided that the current density stratification of the circumstellar gas (i.e. shocked shell and unperturbed AGB shells) is determined. The density of the ionised part of the shell is estimated from the equation of state of a perfect gas, assuming a constant electron temperature T_e (typically 10 000 K).

Then, the ionised masses for both H and He^+ are derived assuming equilibrium between ionisation and recombination events. It means, that within a certain volume, limited by the Strömgren radius R_{ion} , the rate of recombinations to all levels but the ground state, is equal to the number of ionising photons from the central star. This condition translates into

$$Q(\text{H}^0) = 4\pi \int_{R_*}^{R_{\text{ion}}(\text{H}^+)} \alpha_{\text{B}}(\text{H}^0) r^2 N_{\text{e}} N(\text{H}^+) dr \quad (26)$$

for neutral hydrogen and

$$Q(\text{He}^+) = 4\pi \int_{R^*}^{R_{\text{ion}}(\text{He}^{++})} \alpha_B(\text{He}^+) r^2 N_e N(\text{He}^{++}) dr \quad (27)$$

for single-ionised helium. It is clear that these equations may be fulfilled as long as $R_{\text{ion}} \leq R_{\text{neb}}$, where R_{neb} is the outermost radius of the gaseous nebula. The quantities α_B are the effective recombination coefficients, expressing the total recombination rates ($\text{cm}^3 \text{ s}^{-1}$) to all excited levels. They depend weakly on the electron temperature T_e and can be expressed as

$$\begin{aligned} \alpha_B(\text{H}^0) &= 2.54 10^{-13} (T_e/10^4)^{-0.791} \\ \alpha_B(\text{He}^+) &= 1.52 10^{-12} (T_e/10^4)^{-0.716}. \end{aligned} \quad (28)$$

according to the fitting formulas presented by Oliva & Panagia (1983).

We assume that the ionisation radius for single-ionised helium coincides with that of ionised hydrogen, i.e. $R_{\text{ion}}(\text{He}^+) = R_{\text{ion}}(\text{H}^+)$, which is a good approximation for $T \gtrsim 4 \times 10^4 \text{ K}$ (Osterbrock 1974). Then, denoting by $N(\text{H})$ and $N(\text{He})$ the total number densities (neutral atoms + ions; in cm^{-3}) of hydrogen and helium, and by N_e the number density of free electrons, we adopt the following scheme for the ionisation structure (with obvious meaning of the particle number densities N):

$$\begin{cases} N(\text{H}^0) = N(\text{He}^0) = N(\text{He}^+) = 0 \\ N(\text{H}^+) = N(\text{H}) \\ N(\text{He}^{++}) = N(\text{He}) \\ N_e = N(\text{H}) + 2N(\text{He}) \end{cases} \quad (29)$$

for $r < R_{\text{ion}}(\text{He}^{++})$;

$$\begin{cases} N(\text{H}^0) = N(\text{He}^0) = N(\text{He}^{++}) = 0 \\ N(\text{H}^+) = N(\text{H}) \\ N(\text{He}^+) = N(\text{He}) \\ N_e = N(\text{H}) + N(\text{He}) \end{cases} \quad (30)$$

for $R_{\text{ion}}(\text{He}^{++}) \leq r < R_{\text{ion}}(\text{H}^+)$, and

$$\begin{cases} N(\text{H}^0) = N(\text{H}) \\ N(\text{H}^+) = N(\text{He}^+) = N(\text{He}^{++}) = 0 \\ N(\text{He}^0) = N(\text{He}) \\ N_e = 0 \end{cases} \quad (31)$$

for $r > R_{\text{ion}}(\text{H}^+)$.

2.7. Shell thickening due to ionisation

An implicit assumption of the interacting-winds model (outlined in Sects. 2.4.1 and 2.4.2) is that the shocked shell is thin compared to its radial extent, i.e. $\Delta R_S/R_S \ll 1$. However, observations indicate that ring-like nebulae exhibit a large range of relative thickness (from about 0.2 to 0.8, with the peak of the distribution at $\sim 0.4 - 0.5$), and even homogeneous nebulae lacking a central hole exist (Zhang & Kwok 1998). Moreover, the expansion velocities of many young PNe can be notably high, up to $\sim 50 \text{ km s}^{-1}$ (e.g. Weinberger 1989), which is something

not predicted in the framework of the simple interacting-winds model.

Hydrodynamical models of planetary nebulae (Marten & Schönberner 1991) have pointed out that these observations can be explained considering the dynamical effects caused by the ionisation of the nebula. In fact, thanks to the growing number of free electrons the thermal pressure increases inside the ionised nebula, which then tends to expand both inward and outward. As a consequence, the inner and outer nebular rims are decelerated and accelerated, respectively.

Such dynamical effect is included in this model following the analytical treatment suggested by Kahn (1983). The basic steps are shortly recalled below. In practice, the effect of ionisation is treated as a linear perturbation of the equations of momentum and energy conservation (Eqs. 18–19), by introducing a term ΔP_{ion} for the extra pressure. Once the unperturbed solution of the set of Eqs. (16) – (19) is singled out (in the thin-shell approximation), proper first-order corrections are then applied to the radial coordinate R_S and velocity V_S of the contact discontinuity according to the following scheme.

Let us assume that, as a consequence of the pressure contribution due to ionisation, the neutral shell expands outward to a radius $R_S + \Delta R_a$ (with $\Delta R_a > 0$), and the contact discontinuity expands inward down to a radius $R_S + \Delta R_b$ (with $\Delta R_b < 0$), where R_S refers to the unperturbed value. Then, the unperturbed energy equation

$$\frac{d}{dt}(2\pi R_S^3 P) = \frac{1}{2}\dot{m}v^2 - 4\pi R_S^2 P \frac{dR_S}{dt} \quad (32)$$

becomes

$$\begin{aligned} \frac{d}{dt}[2\pi(R_S + \Delta R_b)^3(P + \Delta P_{\text{ion}})] &= \\ \frac{1}{2}\dot{m}v^2 - 4\pi(R_S + \Delta R_b)^2(P + \Delta P_{\text{ion}}) \frac{d(R_S + \Delta R_b)}{dt} \end{aligned} \quad (33)$$

An analogous treatment is applied to the unperturbed momentum equation. The relationship between R_a and R_b is given by equation 31 in Kahn (1983) to whom we refer for all details. Expliciting the time derivatives and neglecting the second-order terms, one eventually derives the radius corrections (ΔR_a , ΔR_b), the velocity corrections ($\dot{\Delta}R_a$, $\dot{\Delta}R_b$), and the pressure corrections ΔP_{ion} , $\dot{\Delta}P_{\text{ion}}$ as a function of the unperturbed quantities, winds parameters and ionised mass.

For the sake of clarity, we can now summarise our prescriptions. As the ionisation front breaks into the shocked shell, this latter will be characterised by three relevant radii, namely:

$$R_S^* = R_S + \Delta R_b : \text{actual contact discontinuity} \quad (34)$$

$$R_{\text{ion}} = R_S + \Delta R_a : \text{ionisation front} \quad (35)$$

$$R_{\text{out}} = \left[R_{\text{ion}}^3 + \frac{3M_{\text{neut}}}{4\pi\rho_{\text{neut}}} \right]^{1/3} : \text{outer radius of the shell} \quad (36)$$

The outer radius R_{out} of the neutral part of the shell – with mass $M_{\text{neut}} = M_S - M_{\text{ion}}$ – is calculated assuming a

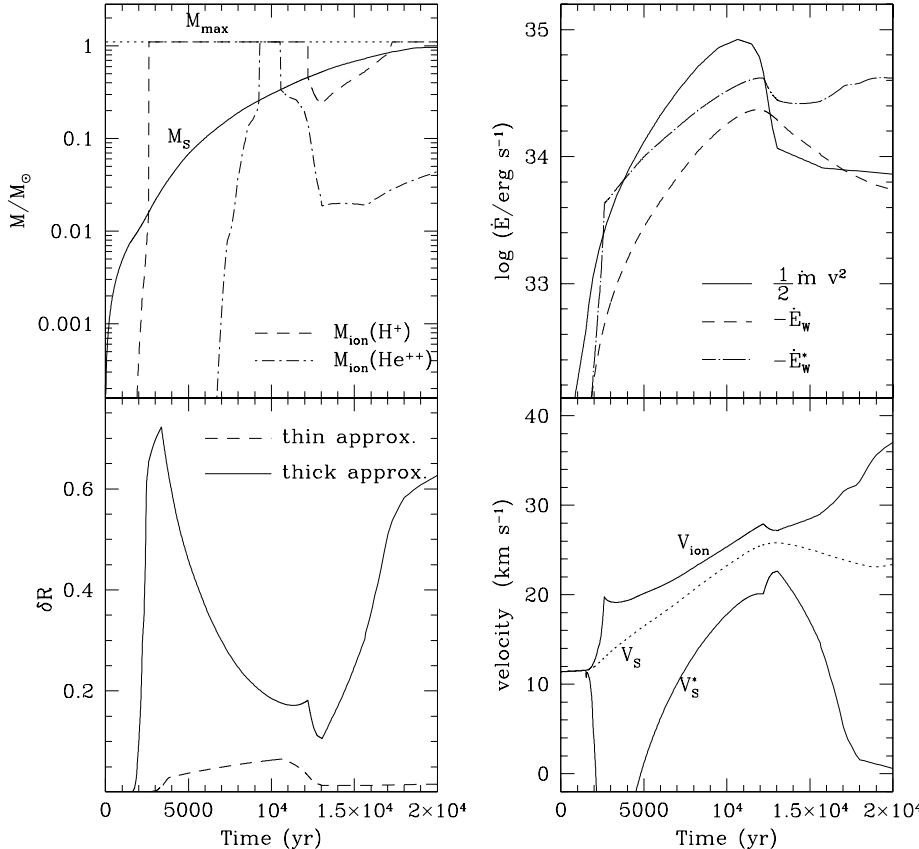


Fig. 9. Predicted properties of the shocked nebula as a function of time, accounting for the dynamical effect resulting from ionisation (model 4 in Table 2). **Top-left panel:** Temporal behaviour of the mass of the shocked shell M_s , and ionised masses for H^+ and He^{++} . The total mass M_{\max} of the circumstellar AGB ejecta is also shown (dotted line). **Top-right panel:** Comparison between the rate of injection of mechanical energy from the fast wind ($\frac{1}{2}mv^2$), and the rate of the work done by the pressure in expanding the shell ($-\dot{E}_W$, $-\dot{E}_W^*$; see text). **Bottom-left panel:** Relative thickness δR of the ionised part of the shocked shell. The prediction under the thin-shell approximation is compared to the case in which the shell thickening due to ionisation is included. **Bottom-right panel:** Velocities at the shell boundaries: V_s of the contact discontinuity under the thin-shell approximation (dotted line); V_s^* of the actual contact discontinuity, and V_{ion} of the ionisation front (solid lines) when the shell-thickening corrections are included. See text for more details

uniform average density ρ_{neut} , which is derived from the equation of state of perfect gas, assuming a temperature of 100 K. In this case the isothermal speed of sound is typically of 1 km s^{-1} .

In general, we have $R_s^* \leq R_{\text{ion}} \leq R_{\text{out}}$, the first and second equalities corresponding to the cases of complete shell neutrality ($M_{\text{neut}} = M_s$) and ionisation ($M_{\text{neut}} = 0$), respectively.

Moreover, it follows that the expansion of the ionised part of the shell produces a deceleration of the actual contact discontinuity that will expand with a velocity

$$V_s^* = V_s + \Delta \dot{R}_b \quad (\text{with } \Delta \dot{R}_b < 0), \quad (37)$$

and an acceleration of the ionisation front that will move outward with a velocity

$$V_{\text{ion}} = V_s + \Delta \dot{R}_a \quad (\text{with } \Delta \dot{R}_a > 0) \quad (38)$$

It should be noticed that such a first-order perturbation approach is strictly correct only as long as $\Delta R_b \ll R_s$, i.e. during the early stages of the expansion when a small fraction of the shell is ionised. Moreover, with the above prescriptions we implicitly suppose that there is a pressure equilibrium and homogeneity in the ionised

part of the shell. This assumption is acceptable considering that a rarefaction wave, generated by the initial inward motion of the contact discontinuity, is expected to rapidly homogenise the gas (Breitschwerdt & Kahn 1990). It is also clear that the adopted treatment is a very simplified approximation of the real phenomenon. Nevertheless, comparing our results with both the predictions of hydrodynamical models and observed data, we generally find a good agreement (see Figs. 9 and 17).

An example of the application of the shell-thickening approximation is shown in Fig. 9, that refers to a model nebula surrounding a central star with mass of $\sim 0.6 M_{\odot}$, and initial solar metallicity.

The relative thickness of the ionised shell

$$\delta R = \frac{R_{\text{ion}} - R_s^*}{R_{\text{ion}}} \quad (39)$$

is shown as a function of time (solid line, bottom-left panel), and compared to that expected according to the thin-shell approximation (dashed line). The latter curve is derived by integrating Eqs. (16) – (19), and assuming that the gas density in the ionised shocked shell is a factor $k = 5$ times larger than the density of the unperturbed AGB wind, i.e. $\rho_{\text{ion}} = k \dot{M}_{\text{AGB}} / (4\pi R_s^2 V_s)$, as suggested by

VK85.¹ In this case the thickness slowly increases with time, being mostly below 0.1.

On the contrary, when the pressure contribution due to ionisation is taken into account, the shocked shell progressively thickens as the ionisation front breaks into it, reaching a maximum of $\delta R \sim 0.7$ when the whole shell is ionised. Actually, at this stage, the ionisation front out-passes the outer rim of the shocked shell and embraces the undisturbed low-density AGB wind completely (see top-left panel of Fig. 9).

After the maximum of δR , its subsequent decline and further increase can be understood considering the competition between the rates of i) the mechanical energy input from the fast wind – which tends to compress the shell from the back (term $\dot{m}v^2/2$) – and ii) the work done by the pressure to expand the shell. The latter is expressed by the term $-\dot{E}_W = 4\pi PR_S^2 V_S$ for the unperturbed case, and the equivalent term $-\dot{E}_W^* = 4\pi(P + \Delta P_{\text{ion}})(R_S + \Delta R_b)^2(V_S + \Delta R_b)$ when the first-order corrections are applied. As shown in Fig. 9 (top-right panel), as long as the first term dominates, the shell thickness decreases; at later times it starts to increase again, as the kinetic energy input of the fast-wind drops and the adiabatic expansion prevails.

Similar considerations can be applied to explain the temporal behaviour of the velocity at the inner and outer rims of the ionised nebula (bottom-right panel). The increase of the pressure inside of the ionised shell determines the initial strong acceleration of the ionisation front and the deceleration of the contact discontinuity (which may even attain negative values corresponding to a short-lived inward motion). The subsequent acceleration of both rims (the shell is now fully ionised) is driven by the increasing pressure of the hot bubble. Finally, when the strength of the fast wind weakens, the contact discontinuity and the outer rim of the nebula are decelerated and accelerated, respectively, while the ionised gas tends to expand both inward and outward. We can note that the velocities attained at the same time by the shell rims can be quite different, and cover the wide range of observed velocities in PNe, typically from few km s^{-1} to $30 - 40 \text{ km s}^{-1}$.

The reliability of these predictions can be checked by comparison with the results of hydrodynamical calculations from Marten & Schönberner (1991). As far as the shell thickening is concerned, it is encouraging to note that the temporal behaviour of δR shown in Fig. 9 closely resembles the predictions of their numerical simulations (see figure 10 in Marten & Schönberner). The evolution of the rim velocities – i.e. the acceleration of the ionisation front and deceleration of the contact discontinuity during the early stages of the ionisation phase – is also recovered by our analytical model.

¹ $k = 5$ is indicated by VK85 as a reasonable compromise between the high density contrast generated by a isothermal shock and the density decrease in the ionised nebula

2.8. Optical properties of the nebulae

With the aid of the prescriptions given in Sect. 2.6, we are able to determine not only the ionised masses for H^+ , He^+ , and He^{++} at each time step during the post-AGB evolution, but we can also naturally discriminate between *optically thick* and *optically thin* configurations, depending on whether the continuum photons (relative to a given ion) are partially or totally absorbed by radiative recombination transitions in the nebula. To this aim, we calculate at each time during the evolution the *absorbing factor* (as defined by Méndez et al. 1993)

$$\mu = \frac{N_\nu^{\text{abs}}}{N_\nu^{\text{em}}} \quad (40)$$

giving the fraction of the continuum emitted photons that is actually absorbed by the ion species under consideration. In practice, it can be expressed as the ratio between the ionisation rate Q and the recombination rate within the Strömgren radius, R_{ion} (see Eqs. 26 – 27). It follows that $\mu = 1$ as long as $R_{\text{ion}} \leq R_{\text{neb}}$, which corresponds to the optically thick case. On the other hand, if no radial coordinate, up to R_{neb} , can be found where the equilibrium condition is satisfied – so that R_{ion} cannot be formally defined –, we have $\mu < 1$, which corresponds to the optically thin case. Figure 10 illustrates how the nebular optical properties in both H and He^+ continua are predicted to vary as a function of time as the central star evolve on its post-AGB track.

As far as the H^+ continuum is concerned, we can see that when the central star becomes hot enough to ionise the H atoms, the nebula is expected to be initially optically thick. The transition to the optically-thin configuration occurs as the effective temperature keeps increasing along the horizontal part of the track and the number of the emitted ionising photons is growing. At this stage the whole nebula is ionised. In proximity to the knee of the track (the point of maximum temperature), μ attains its minimum value, implying that a large number of photons are escaping from the ionised nebula. Subsequently, the luminosity starts to drop, the photoionisation rate decreases (hence μ increases), and the nebula becomes optically thick again.

Later on, a second conversion to the optically-thin configuration occurs, being essentially the result of the dynamical expansion of the nebula. In fact, when the gas density gets low enough, recombination in the whole nebula becomes less efficient (in terms of rate of events) than photoionisation.

The optical properties in the He^{++} show notable differences compared to the case of H^+ . First, helium starts to be doubly ionised at quite high effective temperatures (typically $T_{\text{eff}} \sim 60\,000 \text{ K}$). Second, the optically-thin configuration is very short-lived, and restricted to the knee of the track. This reflects the fact that the photoionisation rate for He^+ is systematically lower than that for H (see Fig. 8), and presents a much steeper decrease with effective temperature and luminosity.

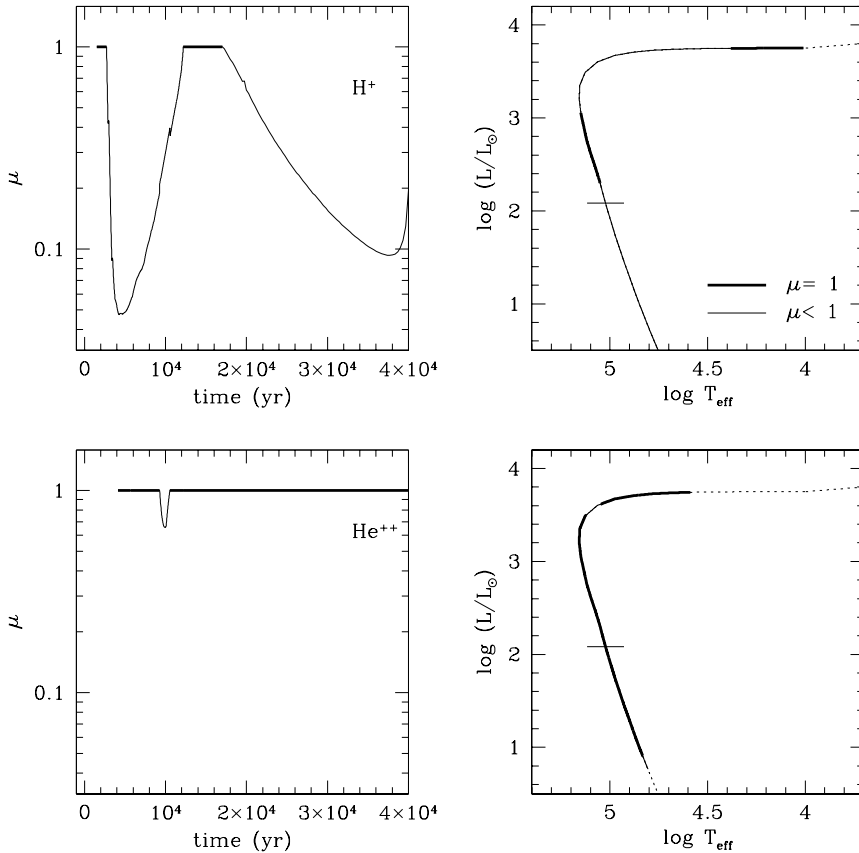


Fig. 10. Expected optically thick and thin configurations during the evolution of a PN ionised by a central star with a mass of $\sim 0.6M_{\odot}$ and initial solar composition (model 4 in Table 2). **Left panels:** absorbing factor μ (given by Eq. 40) as a function of time for both H^+ and He^{++} ions (top and bottom panels, respectively). Time is set to zero at the end of the AGB evolution. **Right panels:** Predicted optical appearance of the nebula as the central star evolves along the post-AGB track on the H-R diagram. The adopted notation is as follows: dotted line as long as the photoionisation rate $Q < 10^{40} \text{ s}^{-1}$; solid lines for optical thick ($\mu = 1$) or thin ($\mu < 1$) configurations as indicated. The horizontal mark on the tracks corresponds to the evolutionary age of 4×10^4 yr, which corresponds to the limit of the interval shown in the left plots

Finally, it is worth remarking that in our model ionisation and optical properties of PNe are predicted according to a coherent coupling between the evolution of the central star and the dynamics of the nebula. This represents an important improvement upon past synthetic approaches, that in many cases lack any dynamical description of the nebulae (e.g. Stanghellini & Renzini 2000) and/or adopt μ as free parameter (e.g. Méndez & Soffner 1997).

2.9. Intensities of few relevant optical emission lines

We aim at predicting the nebular luminosities at the wavelengths of a few important lines typically observed in PNe, namely: the recombination lines $\text{H}\beta \lambda 4861$ and $\text{He II} \lambda 4686$, and the nebular forbidden line $[\text{O III}] \lambda 5007$.

As a first approach, the intensities of these lines are calculated by standard procedures (as described below), under simple but reasonable assumptions for the physical conditions of the emitting regions. Specifically, we assume that the temperature T_e and density N_e of free electrons are constant. In particular, N_e is predicted according to the ionisation structure described by Eqs. (29) – (31), whereas T_e is considered a free input parameter, which is chosen in the typical range indicated by observations, that is $8000 \text{ K} \lesssim T_e \lesssim 15000 \text{ K}$.

These assumptions may be considered completely satisfactory as far as recombinations lines are concerned,

as they depend mostly on atomic parameters and only weakly on T_e . The case of forbidden lines is more delicate, due to their high sensitiveness the electron temperature which cannot be predicted but has to be assumed by the model. It is clear that an improved description of the line emission from PNe can be attained only with the aid of a photoionisation code. However, our choice should represent a reasonable first step, and should be adequate to the purpose of exploring the sensitiveness of PNe properties to various possible physical conditions.

2.9.1. The recombination lines: $\text{H}\beta$ and $\text{He II} \lambda 4686$

The evaluation of the total luminosity L_{λ} emitted by the ionised nebula in a particular recombination transition (of wavelength λ) requires the calculation of

$$L_{\lambda} = 4\pi \int_{R^*}^{R_{\text{ion}}} J_{\lambda}(r) r^2 dr \quad (41)$$

where the integral is performed over the Strömgren volume of the ion under consideration, with

$$J_{\lambda} = \alpha(nn') N_e N_{\text{ion}} h\nu \quad (42)$$

being the volume emission ($\text{erg cm}^{-3} \text{ s}^{-1}$), and $\alpha(nn')$ denoting the recombination coefficient of the transition from state n to state n' .

This latter parameter is calculated adopting the fitting relations presented by Péquignot et al. (1991), as a function of T_e and ionic charge, for both the recombination H β line of H at $\lambda = 4861 \text{ \AA}$ [$\alpha_{\text{H}^+}(4, 2)$], and the recombination line of He II at $\lambda = 4686 \text{ \AA}$ [$\alpha_{\text{He}^{++}}(4, 3)$].

All other quantities in the above equations are known once the ionisation structure of the nebula is determined following the prescriptions described in Sect. 2.6.

2.9.2. The forbidden line: [O III] $\lambda 5007$

The intensity of this nebular line – corresponding to the transition from the collisionally-excited metastable level $j = {}^1\text{D}_2$ to the level $i = {}^3\text{P}_2$ – is calculated from

$$I_{ji} = A_{ji} N_j \frac{Y(\text{O}^{++})}{Y(\text{O})} \frac{Y(\text{O})}{Y(\text{H})} h\nu_{ji} \frac{n}{1 + Y(\text{He})/Y(\text{H})} \quad (43)$$

(expressed in $\text{erg cm}^{-3} \text{ s}^{-1}$), where $A_{ji} = 0.021 \text{ s}^{-1}$ is the radiative transition probability; $N_j(T_e, N_e)$ is the relative population of level j ; $Y(\text{O}^{++})/Y(\text{O})$ denotes the ionic abundance of O^{++} relative to the total oxygen abundance (in all excitation and ionisation states); $Y(\text{O})/Y(\text{H})$ refers to abundance of oxygen (in all states) with respect to hydrogen; $Y(\text{H})$ and $Y(\text{He})$ are the chemical abundances (by number, in mole gr^{-1}) of hydrogen and helium; and $n = N(\text{H}) + N(\text{He})$ corresponds to the number density (in cm^{-3}) of H and He.

The most critical quantity here is $N_j(T_e, N_e)$, as it depends on both the electron temperature and density. It is determined using the detailed calculations of atomic transitions performed by Kafatos & Lynch (1980), interpolating in T_e and N_e the data of their Table 3E. All other quantities (i.e. elemental abundances and densities) are predicted by our model.

Equation (43) must be integrated over volume to obtain the emitted luminosity in the [O III] $\lambda 5007$ line. We assume that both O^{++} and He^+ ions share the same Strömgren volumes, based on the fact the ionisation potentials of O^{++} (54.9 eV) and He^+ (54.4 eV) are almost identical. In other words, we assume that the emission of the [O III] $\lambda 5007$ line can only originate from regions where He is single-ionised, disappearing as soon as He becomes double-ionised. Moreover, we consider that within that region $Y(\text{O}^{++}) = Y(\text{O})$, which is also a good approximation (Osterbrock 1974).

2.10. Summary of model parameters

Before analysing the expected dynamical and ionisation properties of PNe, it is worth summarising the parameters/prescriptions of the model that are can be varied in our calculations, namely:

- initial metallicity of the stellar progenitor, Z_i ;
- stellar mass at the onset of the TP-AGB phase, $M_{1\text{TP}}$;
- mass of the central star of the PN model, M_{CSPN} ;
- H- or He-burning post-AGB track;
- the transition time, t_{tr} ;

- expansion velocity of the stellar wind during the last stages of the AGB evolution, $V_{\text{AGB}}^{\text{max}}$;
- electron temperature of the ionised shell, T_e .

It is worth remarking that our default set of prescriptions include i) the ionisation fluxes from model atmospheres, and ii) the thick-shell correction scheme. For purpose of comparison, we may easily relax these assumptions adopting the blackbody energy distribution and the thin-shell approximation. This is the case for few examples discussed in the text.

Calculated PNe models are listed in Table 2, so that each reference number N_{mod} corresponds to a particular set of parameters. It is clear that some of these quantities are intrinsic properties of the models (e.g. Z_i , M_{CSPN}), whereas others are genuine free parameters (e.g. t_{tr} , $V_{\text{AGB}}^{\text{max}}$, T_e). The aim is to define suitable ranges for these parameters, on the basis of observations of Galactic PNe. For the other model ingredients, not explicitly mentioned here, we refer to the prescriptions already discussed in Sect. 2.

3. Overview of model predictions

3.1. Summary plots

The several panels in Fig. 11 illustrate the time evolution – during a period of 30 000 yr – of a PN model corresponding to a H-burning central star with a mass of about $0.6 M_{\odot}$. The selected model (number 4 in Table 2) may be considered typical of Galactic PNe. The run of several physical quantities is shown simultaneously, then offering a useful guide to our further discussion. In short, going from top to bottom panels, we present:

1. the evolution of luminosity and temperature for the central star (left; Sect. 2.3), and the corresponding ionisation rates (right; Sect. 2.5);
2. the masses of the shocked shell and ionised regions (left), and the corresponding μ factors (right; Sect. 2.6);
3. the radii (left) and velocities (right) of the shell boundaries (including the radial location of the inner shock) (Sect. 2.7);
4. the line ratios (left) and total luminosities (right) in the main emission lines (Sect. 2.9).

Similar plots are available for all our models, and allow a better interpretation of the different evolutionary features that may be present. A very interesting comparison is provided, for instance, between the H-burning track of Fig. 11, and a model computed with the same set of parameters, but using a He-burning track (number 9 in Table 2). The latter is presented in Fig. 12, for a total period of 55 000 yr. As can be readily noticed, the He-burning track is characterised by a smaller luminosity and slower evolution than the H-burning one, and this determines a substantially different evolution of the nebular properties. For instance, the nebula shown in Fig. 12 is nearly always optically thin

Table 2. Specification of the basic parameters adopted to calculate PN models

N_{mod}	$M_{1\text{TP}}$ (M_{\odot})	M_{CSPN} (M_{\odot})	H-/He- burner	$V_{\text{AGB}}^{\text{max}}$ (km s^{-1})	t_{tr} (10^3 yr)	T_{e} (10^3 K)	notes
1	1.7	0.5989	H	15	1.5	10.0	C
2	1.7	0.5989	H	$f(Z)$	1.5	10.0	C
3	1.7	0.5989	H	$f(L)^*$	1.5	10.0	C
4	1.7	0.5989	H	$f(L)$	1.5	10.0	A, B, C, D, E
5	1.7	0.5989	H	15	0.5	10.0	C, D
6	1.7	0.5989	H	$f(L)$	1.5	10.0	thin-shell approx.
7	1.7	0.5989	H	$f(L)$	1.5	10.0	blackbody
8	1.7	0.5989	H	$f(L)$	8.0	10.0	D
9	1.7	0.5989	He	$f(L)$	1.5	10.0	B, D
10	1.7	0.5989	He	$f(L)$	5.0	10.0	D
11	1.7	0.5989	H	$f(L)$	1.5	8.0	E
12	1.7	0.5989	H	$f(L)$	1.5	12.0	E
13	1.7	0.5989	H	$f(L)$	1.5	13.0	E
14	1.0	0.5577	H	$f(L)$	10.0	10.0	C
15	1.0	0.5577	H	$f(Z)$	10.0	10.0	C
16	1.2	0.5706	H	$f(L)$	1.5	10.0	A, D
17	1.2	0.5706	H	$f(L)$	8.0	10.0	D
18	1.5	0.5868	H	$f(L)$	1.5	10.0	A
19	1.5	0.5868	He	$f(L)$	10.0	10.0	
20	1.8	0.6120	H	$f(L)$	1.5	10.0	A
21	2.0	0.6296	H	$f(L)$	1.5	10.0	A, B, D
22	2.0	0.6296	H	$f(L)$	0.5	10.0	D
23	2.0	0.6296	He	$f(L)$	1.5	10.0	B
24	2.2	0.6529	H	$f(L)$	1.5	10.0	A, D
25	2.2	0.6529	H	$f(L)$	0.5	10.0	D
26	2.5	0.6865	H	$f(L)$	1.5	10.0	A, D
27	2.5	0.6865	H	$f(L)$	0.5	10.0	D
28	2.5	0.6865	H	$f(L)$	0.3	10.0	D
29	3.0	0.7867	H	$f(L)$	0.5	10.0	

Sequences of models with the same set of model parameters, but varying

A: M_{CSPN} (4-16-18-20-21-24-26), (9-16);

B: H-/He-burning post-AGB tracks (4-9), (8-16);

C: $V_{\text{AGB}}^{\text{max}}$ (1-2-3-4-5), (14,15);

D: T_{tr} (4-8),(9-10), (21-22), (24-25), (26-27-28);

E: T_{e} (4,11,12,13).

* According to the original results of Krüger et al. (1994) (i.e. $f_{\text{v}} = 1$; see Sect. 2.2.1); in all other models $f_{\text{v}} = 0.588$ is adopted.

to H-ionising photons ($\mu(\text{H}^+) < 1$), and presents line ratios $[\text{O III}] \lambda 5007/\text{He II} \lambda 4686$ and $\text{He II} \lambda 4686/\text{H}\beta$ that at late times are very different from those predicted for the PN model of Fig. 11. These differences are mainly due to the fact that, in comparison to the H-burning central star, the maximum flux of ionising photons emitted by the He-burning star is attained later (because of the longer evolutionary time-scales), when the nebular material has expanded to larger radii.

3.2. Detection probabilities of different PNe

The relative probability of observing PNe of different progenitors (i.e. stars of different masses, ages, and metallicities) constitutes a basic aspect in the interpretation of PNe data. As briefly mentioned in Sect. 1, the highest probabilities of observing the PN stage should be reached

when we have a suitable combination between the evolutionary time-scale of the central star, and the dynamical time-scales of the expanding nebulae: A fine tuning between the two can increase either the lifetime or the surface brightness of a PN, both factors enhancing the detection probability.

Actually, the problem of determining a “detection probability” is much more complex. For instance, in the case of distant (point-like) nebulae, the detection probability should correlate with the absolute luminosity, rather than with the surface brightness. Also the choice of the detection method is crucial in determining which PNe will be better sampled by a given survey. Since our models predict a lot of different properties of PNe, we are also able to face this question in a more generic way: we can construct synthetic samples of PNe containing all their basic observable properties, which are then be filtered adopting

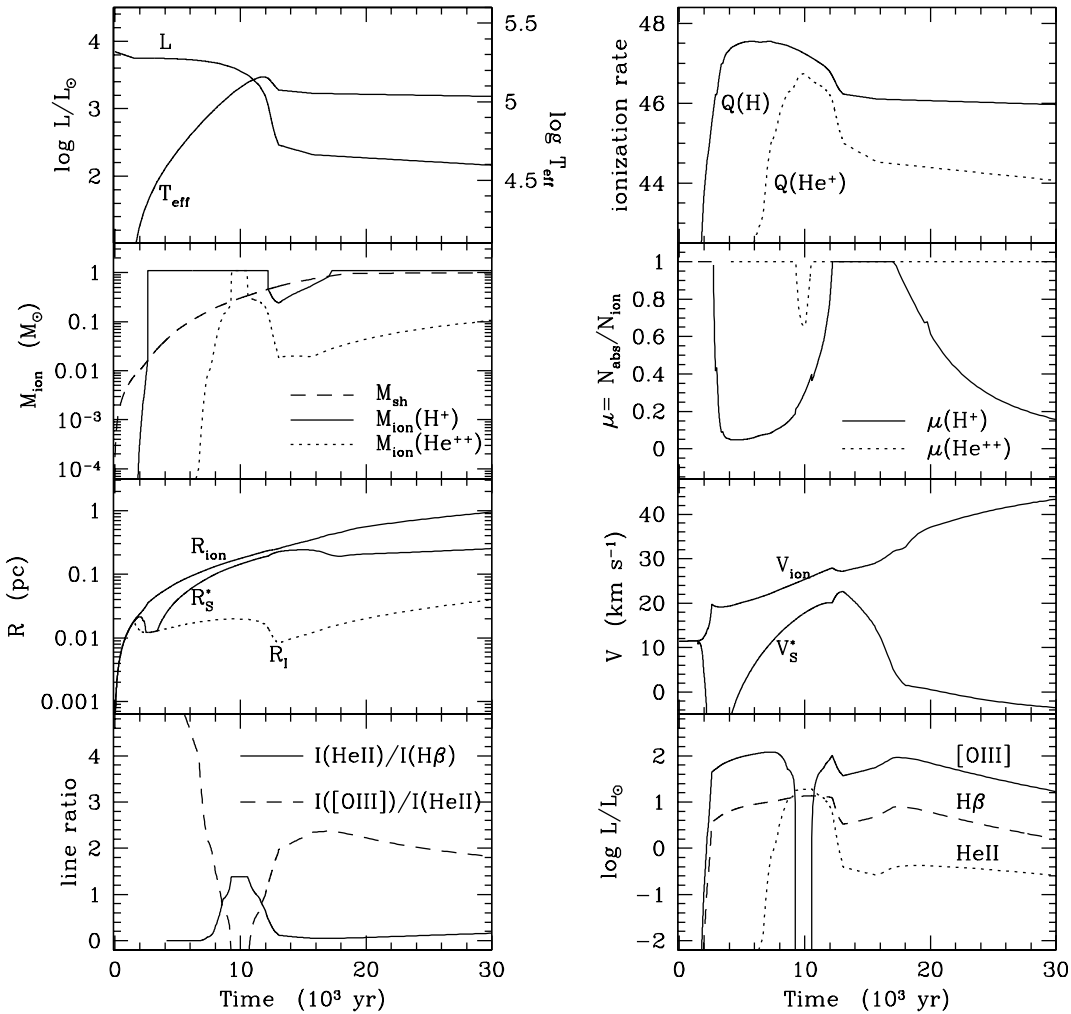


Fig. 11. Predicted evolution of basic parameters corresponding to a PN model ionised by a H-burner central star with mass of $\sim 0.6 M_{\odot}$ (model 4). See Sect. 3 for a description

some given observational criteria. Developing such a tool, however, is beyond the scope of this paper.

Anyway, it is worth getting a first insight into the problem. To this aim, in Fig. 13 we plot the evolution of two PNe models in the HR diagram, corresponding to H- and He-burning tracks (models 4 and 9, respectively). Along the tracks, we mark the CSPN position at equally spaced intervals of age (700 yr) by means of circles whose area is proportional either to the emitted line luminosity L_{λ} (left panels) or to the PN average surface brightness S_{λ} (right panels) in a given emission line (either $H\beta$ or $[O\text{III}] \lambda 5007$). S_{λ} is simply assumed to be proportional to the quantity $L_{\lambda}/R_{\text{ion}}^2$, where R_{ion} is the total nebular radius.

The figure gives a clear indication of the regions of the HR diagram where these PNe are more likely to be found, as well as of their relative luminosities and surface brightnesses. In the case of the H-burning track, the probability of detection in the $H\beta$ line should be more or less evenly distributed in effective temperature, as long as $\log T_{\text{eff}} \gtrsim 4.2$ and the CSPN is crossing the HR diagram horizontally: In this part of its evolution, the nebula

evolves at slightly increasing $L_{H\beta}$, and slightly decreasing $S_{H\beta}$. Also, there is a non-negligible probability of finding these PNe at later ages, when their central stars reach the initial part of the white dwarf cooling sequence (at $\log L/L_{\odot} \simeq 2.3$, $\log T_{\text{eff}} \simeq 5.05$) and the evolutionary speed slow down. However, in this part of the HR diagram, $S_{H\beta}$ is extremely low.

The same H-burning nebula should be much brighter in the $[O\text{III}] \lambda 5007$ line. Remarkably, during the horizontal crossing of the HR diagram, the detection of $[O\text{III}]$ would be favoured in a more limited temperature interval, i.e. $5.0 \gtrsim \log T_{\text{eff}} \gtrsim 4.2$; at higher temperatures, the $[O\text{III}]$ line temporarily disappears. This effect is caused by the photoionisation of O^{++} into O^{+++} , and is explained in more detail in Sect. 4.6.

Figure 13 also illustrates the striking differences between the H- and He-burning cases. The PN with the He-burning track have line luminosities that are just slightly lower than its H-burning counterpart. However, except for the very initial stages, the He-burning model presents much lower surface brightnesses. This is caused by the

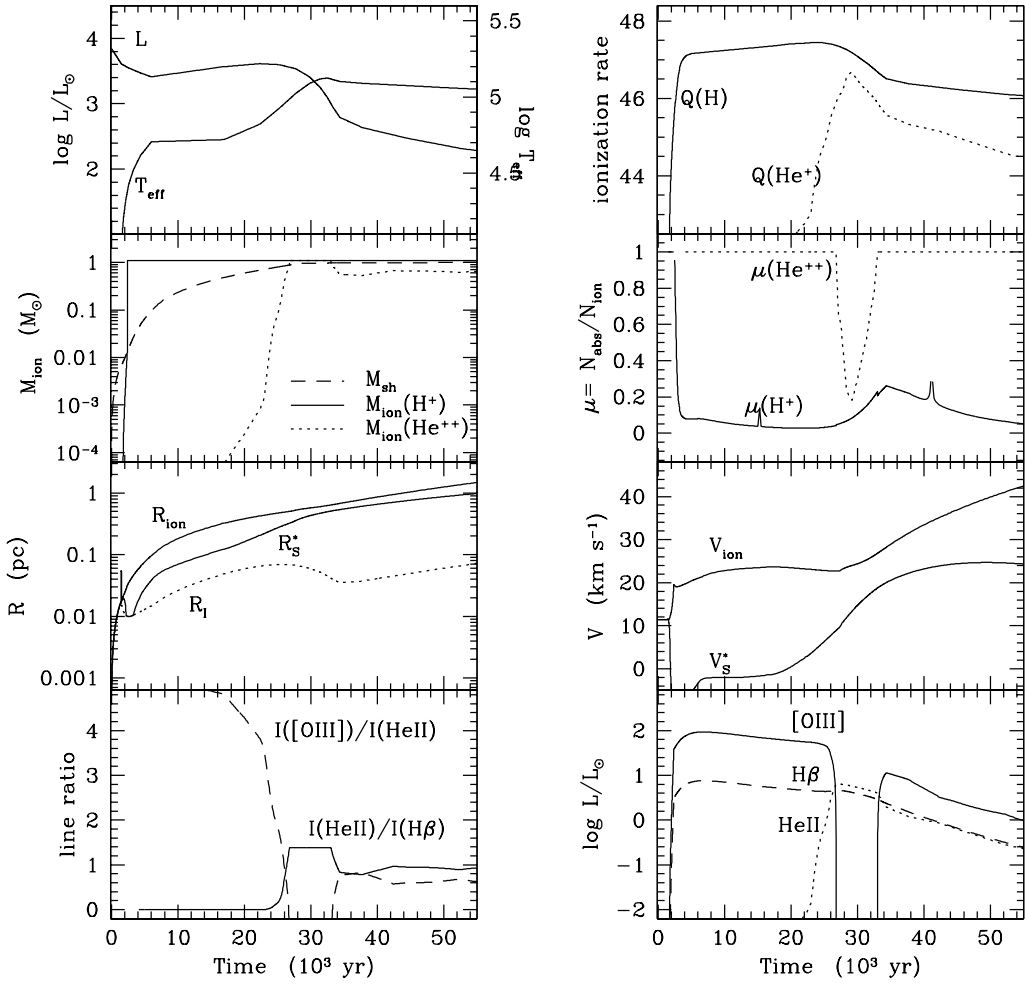


Fig. 12. The same as in Fig. 11, but for a He-burner central star with mass of $\sim 0.6 M_\odot$ (model 9)

longer evolutionary time-scales of the He-burning central stars. Moreover, the He-burning CSPN makes a long pause in its evolution amid the horizontal crossing of the HR diagram, at $T_{\text{eff}} \simeq 4.7$, period in which the nebula should have a very high probability of being detected. During this pause, the line luminosity is almost constant, but the surface brightness decreases a lot, due to nebular expansion. Thereafter, the CSPN resumes its evolution at a slower pace than in the H-burning case. In summary, PN with He-burning tracks should present a very odd distribution in the HR diagram: most of them should concentrate in the $\log T_{\text{eff}} \gtrsim 4.7$ region, with a small fraction of high-surface brightness objects appearing at $4.7 \gtrsim \log T_{\text{eff}} \gtrsim 4.3$. This trend should be present in both $H\beta$ and $[\text{O III}] \lambda 5007$ lines. However, similarly to the H-burning case, the $[\text{O III}]$ line disappears in the upper-left section of the HR diagram, when $T_{\text{eff}} \gtrsim 4.9$ and $\log L/L_\odot \gtrsim 3$.

4. Comparison with observations

The next sections are dedicated to present the results of PNe model calculations in comparison to the observed data, which are used to both calibrate the free parameters and, more generally, test the theoretical prescriptions. As to the calibration of the parameters, we restrict the comparison here to a sample of Galactic PNe, so as to minimise possible population effects (due e.g. to different mean metallicity) that may be present among PNe samples of nearby galaxies.

4.1. The ionised mass – nebular radius relationship

PNe display a positive correlation between the ionised mass and the nebular size, which is shown in Fig. 14 for Galactic PNe. Such relation offers also a method to estimate the distance of PNe, once the ionised mass and the angular radius can be measured (Maciel & Pottasch 1980; see also Kwok 1985). The mass-radius relationship is naturally explained in the framework of the interacting-winds

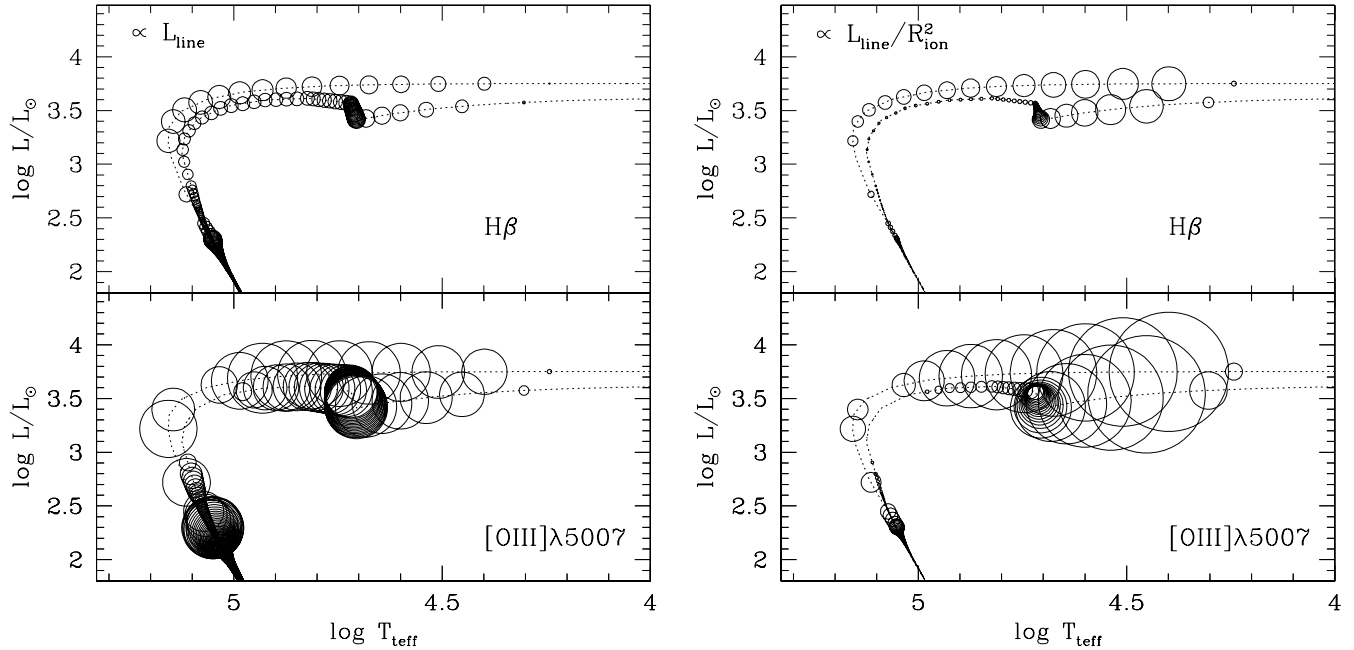


Fig. 13. Representation of the relative probabilities to detect a PN observed either in $H\beta$ (top panel) or in the $[O\text{III}]\lambda 5007$ line (bottom panel), as its central star evolves along its post-AGB track, assumed either H-burning (model 4) or He-burning (model 9, that corresponds to the least luminous track in each panel). Circles are drawn at equally-spaced time intervals of 700 yr, their area being proportional to the current values of the luminosity (left panels), and surface brightness (right panels) in each emission line

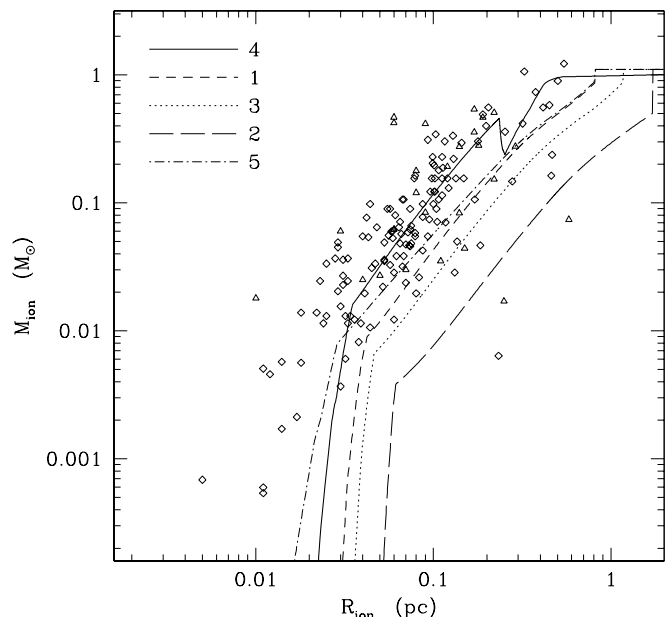


Fig. 14. Ionised mass – nebular radius relationship. Observed data for Galactic PNe are taken from the compilation by Zhang (1995; squares), and the sample presented by Boffi & Stanghellini (1994; triangles). Model predictions are displayed for various prescriptions for $V_{\text{AGB}}^{\text{max}}$ and t_{tr} (see Table 2)

model (VK85), which couples the dynamical expansion of the nebula with the ionising properties of the central star.

In this study we use the observed relation first to derive some calibration of $V_{\text{AGB}}^{\text{max}}$, for which we presented three possible prescriptions in Sect. 2.2.1. To this aim, we calculate PN models all corresponding to a CSPN with mass of about $0.6 M_{\odot}$, since this should be representative of the typical PN population in the Galactic disk (see Stasińska et al. 1997, and references therein). The resulting values for $V_{\text{AGB}}^{\text{max}}$ are: i) $\text{const.} = 15 \text{ km s}^{-1}$ (models 1 and 5), ii) $F(Z) \sim 27 \text{ km s}^{-1}$ (model 2) according to Bressan et al. (1998), with Z being the effective metal abundance (higher than the initial value because of dredge-up episodes); iii) $F(L) \sim 18 \text{ km s}^{-1}$ (model 3) according to Krüger et al. (1994). We can notice that all the corresponding curves in Fig. 14 lie below the mean line of the observed data, even when a shorter transition time ($t_{\text{tr}} = 500$ yr, model 5) is adopted to reduce the discrepancy.

We find that the mean mass-radius relation can be well reproduced by decreasing $V_{\text{AGB}}^{\text{max}}$, e.g. applying a multiplicative factor $f_v = 0.588$ to the original Krüger et al. data (so that $V_{\text{AGB}}^{\text{max}} \sim 10 \text{ km s}^{-1}$ in model 4; see also Fig. 1). Most of our PN model calculations, presented in the next sections, are carried out by adopting this calibrated prescription. An additional advantage, compared to the case of a constant velocity, is that such a choice produces a natural dispersion of the expansion velocities at the end of AGB, which seems more consistent with the observed scatter of the expansion velocities of young PNe at small radii (see Fig. 21).

With this calibration for $V_{\text{AGB}}^{\text{max}}$, we show in Fig. 15 the predictions for several choices of the other model param-

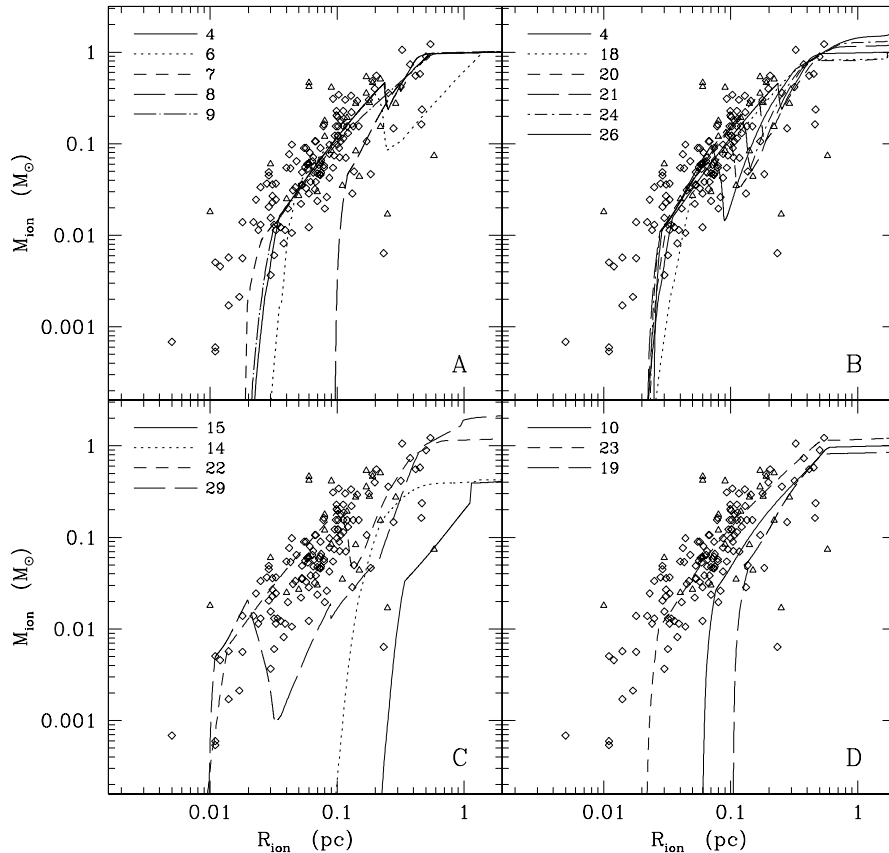


Fig. 15. Ionised mass - nebular radius relationship. Observed data are the same as in Fig. 14. Theoretical predictions are shown for several choices of the parameters (see Table 2)

eters (quoted in Table 2). In general, all tracks exhibit a common feature in the $M_{\text{ion}} - R_{\text{ion}}$ plane, i.e. a change in the slope after an initial steep increase of the ionised mass. This point marks the transition from ionisation- to density-bounded shell configurations. In other words, during the early epochs the ionisation front proceeds forward but keeping behind the outer shock, so that the nebula is optically thick to the ionising photons, and the outermost part of the shocked shell is still neutral.

As soon as the ionisation front reaches the outer rim of the shell, the unperturbed (low-density) AGB wind is also ionised and the nebula becomes optically thin to the continuum photons emitted by the central star. During these stages the whole shell is ionised, and the theoretical mass-radius tracks merely represent the evolution of the shell parameters. The almost linear behaviour proceeds until when – due to the decrease of the ionising flux from the central star – the ionised mass starts to decrease as well, and correspondingly the ionisation front recedes inside the shell. At later ages, M_{ion} increases again as the nebula expands and its density decreases. Finally, when the AGB wind is entirely engulfed by the shocked shell, M_{ion} remains constant at increasing radius (horizontal part of the tracks).

The evolution of the optical properties of PNe along a mass-radius track is also shown in Fig. 16, together with the observed data for the sample of Galactic PNe studied

by Méndez et al. (1992), who estimate the μ -factor characterising each object. Both the location and the slope of the theoretical relationship for optically thick/thin sources are in excellent agreement with the observed data.

Clearly, this general trend may be affected by various parameters. Let us first discuss the models illustrated in panel A of Fig. 15, all corresponding to a central star with mass of $\approx 0.6M_{\odot}$. Most of these PNe models account for the mean observed mass-radius relation quite well, which is an expected result as they should be representative of the typical Galactic PNe. For a given transition time ($t_{\text{tr}} = 1500$ yr), the largest differences show up at the lowest and largest values of M_{ion} , whereas the models almost converge during the optically-thin stages. For a significantly longer t_{tr} (8000 yr) the observed data are intercepted by the theoretical track (model 8) only at the largest R_{ion} , since the nebula starts to be ionised when it has already expanded to relatively large dimensions.

The dependence on the mass of the central star can be visualised in panel B of Fig. 15. It turns out that the radius at which ionisation first sets in does not vary much with M_{CSPN} , being essentially determined by the transition time (the same in all models). A clear effect of M_{CSPN} is instead related to the part of the tracks following the transition from optically-thin to optically-thick configurations (the first relative maximum in the curves). At increasing stellar mass, this transition occurs at shorter radii

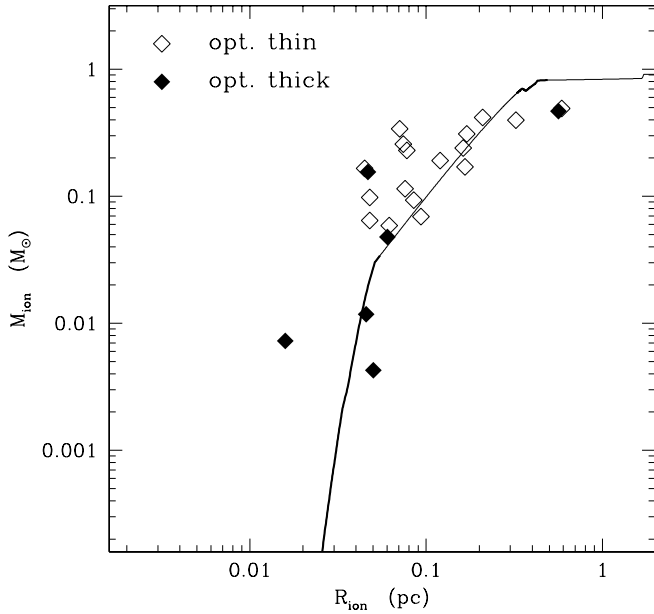


Fig. 16. Ionised mass as a function of the nebular radius for the sample of Galactic PNe analysed by Méndez et al. (1992). Optically-thin/thick sources are distinguished by means of empty/filled symbols, respectively. Along the theoretical track, corresponding to model 18, the expected optical properties are indicated (thick line: optically-thick configuration with $\mu = 1$; thin line: optically-thin configuration with $\mu < 1$)

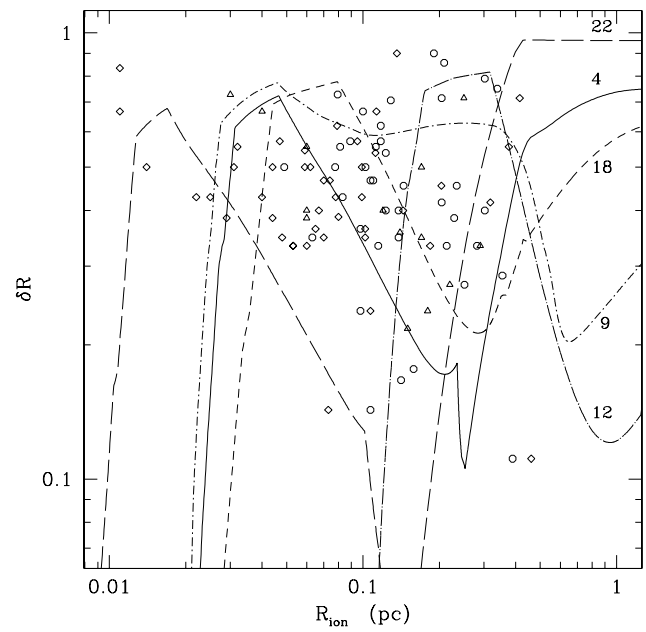


Fig. 17. Relative shell thickness as a function of the nebular radius. Measured radii are taken from Boffi & Stanghellini (1994; triangles); Zhang (1995; squares); and Górný et al. (1997; circles). Corresponding semi-empirical determinations of δR are those derived by Zhang & Kwok (1998). A few theoretical predictions are shown for comparison (see Table 2)

reflecting the faster evolutionary speed. Moreover, we can note that the non-monotonic behaviour of the tracks can explain part of the observed scatter of M_{ion} at given R_{ion} .

The effect of the transition time can be analysed in panel C. In this panel, we can notice that the observed PNe with the lowest masses and radii would be consistent with relatively massive central stars and quite short transition times ($t_{\text{tr}} = 500$ yr; models 22, 29). Models with lower M_{CSPN} and much longer t_{tr} (10000 yr; models 15, 14) succeed in explaining the few data at quite large R_{ion} and relatively low M_{ion} .

Finally, we plot in panel D the expected mass-radius tracks for He-burning post-AGB tracks. These models are consistent with the observed data as well as those with H-burning central stars. Comparing models 21 (H-burner) and 23 (He-burner) – which are calculated with the same set of the other parameters – we can see that, contrary to the H-burning case, in the He-burning model the ionised mass always increases with radius and the nebular shell, once becomes optically thin, remains density-bounded up to the largest radii. This can be explained considering that He-burning tracks are, on average, characterised by quite longer evolutionary time-scales, so that the drop of the ionising flux emitted by the central star occurs when the expanding shell has already reached large radii.

4.2. The nebular shell thickness

PNe exhibit a large variety of morphological and geometrical features (e.g. Schwarz et al. 1992), that clearly cannot be handled by models that assume spherical symmetry. Nevertheless, we can at least test our predictions concerning an important geometrical parameter, namely the relative shell thickness δR (defined by Eq. 39). As already described in Sect. 2.7, our model considers the effect of ionisation in determining the thickness of the shell.

To construct Fig. 17, we combine determinations of nebular radii taken from different sources with the recent semi-empirical determinations of δR (for the primary shell) obtained by Zhang & Kwok (1998) in their morphological analysis of a sample of Galactic PNe. For each of them, Zhang & Kwok (1998) derive relevant morphological parameters, by constraining simulated optical and radio images to reproduce the observed ones. It turns out that δR mostly varies over the range [0.1, 0.8], with a distribution peaked at around 0.45.

We can see that the theoretical predictions (a discussion of the trends is given in Sect. 2.7) account well for the location of the observed data in the δR – R_{ion} plane. Together with the good reproduction of the ionised mass-radius relationship, this fact implies that both the dynamical and ionisation properties of PNe should be reasonably well represented in our model.

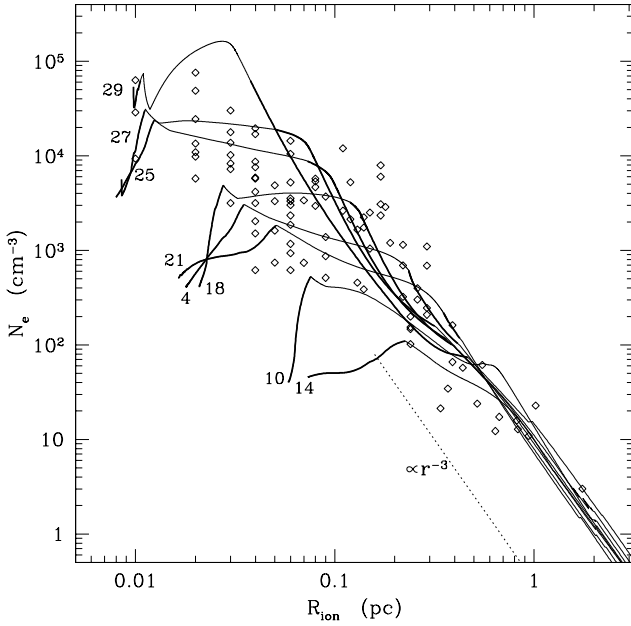


Fig. 18. Electron densities as a function of the nebular size. Observed data for Galactic PNe are taken from the compilation by Phillips (1998). Model predictions are shown for comparison. The straight line, $N_e \propto R_{\text{ion}}^{-3}$, is plotted to indicate the expected slope for constant nebular mass

4.3. Electron densities

Figure 18 displays the radial variation of the nebular electron densities. Empirical determinations of N_e are all derived from the [S II] $\lambda 6717/6730$ forbidden line ratio, which should sample the outer nebular regions. In this way, we expect that the considered PNe sample is little subject to the effects of radial stratification in ionisation and density – present when different lines are used – as well as not dependent on the nebula filling factor, which is the case when N_e is estimated from the radio continuum/H β fluxes.

From the observed distribution of the data points it should be noticed that, first of all, the relation between N_e and R_{ion} shows a relatively large dispersion, which seems to reduce towards larger radii. Second, as pointed out by Phillips (1998), there is clear evidence for a change in the mean slope of the radial gradient at $R_{\text{ion}} \approx 0.1$ pc. Both features are quite well reproduced by our models, showing the evolution of the average density of the ionised shell as function of the radial size of its outer boundary. The data points located at $R_{\text{ion}} < 0.1$ pc would be consistent with a mixture of both optically-thick and thin nebulae, the latter being characterised by a more gradual decrease of N_e with radius. Indeed, this feature would explain the observed scatter of the points at smaller R_{ion} . For $R_{\text{ion}} > 0.1$, the reduced dispersion of the observed data which, on average, seem to follow the relation $N_e \propto R_{\text{ion}}^{-3}$, could be interpreted by the gradual convergence of all PNe to the

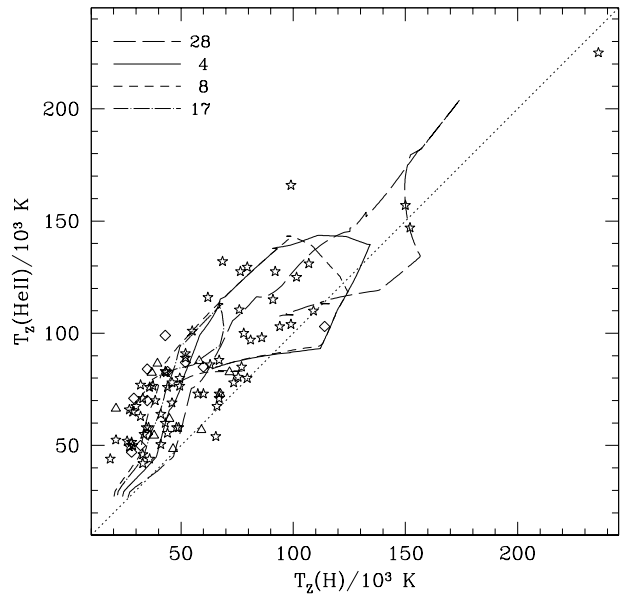


Fig. 19. Zanstra discrepancy between $T_z(\text{H})$ and $T_z(\text{He II})$. Observed data for Galactic PNe are taken from de Freitas Pacheco et al. (1986; triangles); Gleizes et al. (1989; starred symbols); and Méndez et al. (1992; squares). Model predictions for different choices of the parameters are shown for comparison

condition $M_{\text{ion}} = M_{\text{sh}} = \Delta M_{\text{AGB}}$, i.e. the shocked ionised shell embraces all the AGB ejecta, so that its mass remains constant. Finally, we note that the theoretical $N_e - R_{\text{ion}}$ tracks show a systematic trend with the mass of the central star, i.e. at smaller radii the largest densities are attained for more massive CSPN. However, it should be remarked that the predicted N_e refer to average electron densities, which do not account for intrinsic density gradients inside the nebulae.

4.4. PN central stars: temperatures and luminosities

Determining the main parameters of the central stars of PNe, i.e. effective temperature and luminosity, means to cast light on important aspects of both nebular and stellar evolution. For instance, by assigning a position on the H-R diagram to the ionising star, it is possible to derive the stellar mass – from the comparison with theoretical post-AGB tracks – and estimate (an lower limit to) the PN dynamical age, if the expansion velocity and nebular sizes are measured. The combined information on stellar mass and PN age, offers also the possibility to discriminate between H- and He-burning stars (e.g. Dopita et al. 1996).

Unfortunately, the determination of luminosities of Galactic CSPN is indeed problematic, mostly due to the large uncertainties that often affect the observational methods to estimate effective temperatures and distances. The effective temperature of a CSPN can be determined either directly, by fitting observed spectra with model at-

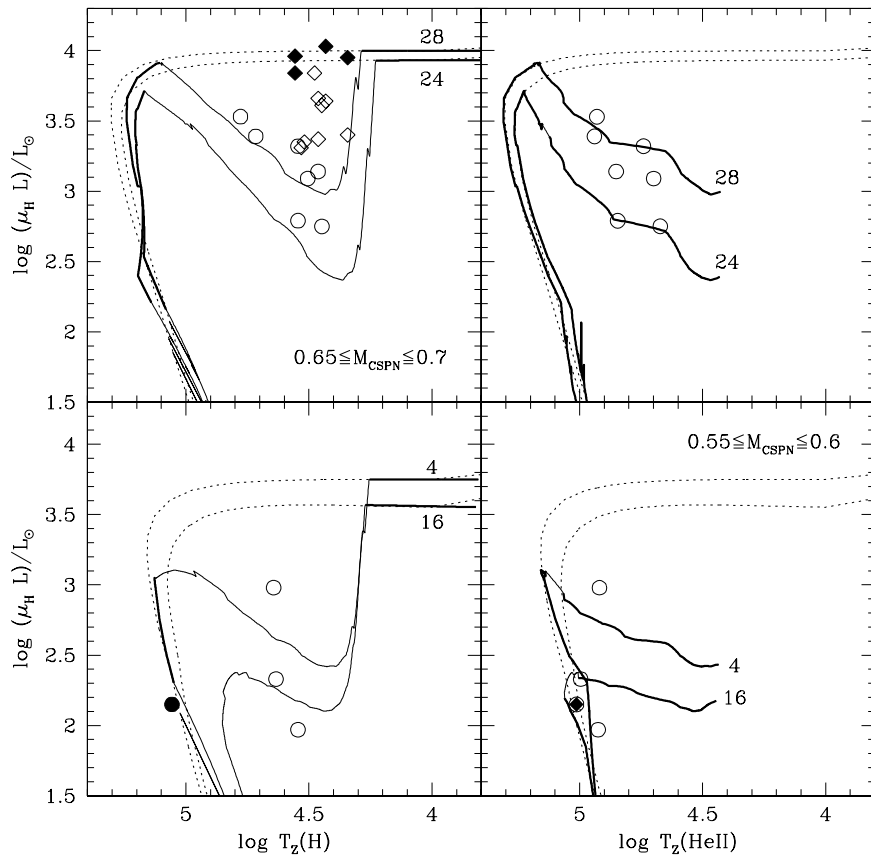


Fig. 20. Zanstra temperatures ($T_Z(H)$ in the left panels and $T_Z(\text{He II})$ in the right ones) and luminosities ($\mu_H L$) of PN central stars. The upper panels present the nebulae with CSPN masses $0.65 \leq M_{\text{CSPN}} \leq 0.7$, whereas the lower panels refer to those with $0.55 \leq M_{\text{CSPN}} \leq 0.6$. Observed data points are taken from Méndez et al. (1992), and shown with filled squares for $\mu_H > 0.7$ and empty squares for $\mu_H < 0.7$. PNe of low-excitation (with $T_Z(H)$ only) and high-excitation (with both $T_Z(H)$ and $T_Z(\text{He II})$) are denoted with squares and circles, respectively. Model predictions are superimposed distinguishing optically-thin/thick configurations (thin/thick solid lines) in the H and He^+ continua, together with the corresponding $\log L - \log T_{\text{eff}}$ tracks (dotted line). The masses of the central stars are chosen consistently with those estimated by Méndez et al. (1992) for the sample PNe

mospheres, or with the aid of indirect methods, such as the Zanstra and energy-balance method (see, e.g., Gathier & Pottasch 1989). The former, first introduced by Zanstra (1931), is based on the assumption that the nebula is optically thick to the ionising continuum under consideration – the H and He II Zanstra temperatures $T_Z(H)$ and $T_Z(\text{He II})$ are usually determined – and requires the measurement of both nebular and central star optical emissions. The latter, first discussed by Stoy (1933), is based on the assumption that the ratio of the total energy emitted by a nebula in forbidden lines to the energy emitted in one of the hydrogen recombination lines depends on the temperature of the central star. Then, once T_{eff} is estimated, the luminosity of the CSPN can be derived, for instance, i) from the apparent magnitude at a given wavelength provided that the distance is known, ii) from the comparison with post-AGB tracks in the $\log g - \log T_{\text{eff}}$ diagram if estimates of the surface gravity g and mass of the CSPN are available; iii) by equating the nebular emission over the whole spectral range to the radiation emission from the central star, with the assumption that the nebula is ionisation-bounded (see, e.g. Gathier & Pottasch 1989, Méndez et al. 1992 for description and application of the methods).

The so-called “Zanstra discrepancy” between $T_Z(H)$ and $T_Z(\text{He II})$ – i.e. usually $T_Z(H) < T_Z(\text{He II})$ – has been a matter of debate for long time (see, e.g., Stasińska &

Tylenda 1986; Gathier & Pottasch 1989; Méndez et al. 1992; Gruenwald & Viegas 2000 and references therein). The discussion aims at identifying the main causes of such discrepancy and their role, namely: i) the condition of optical thinness to the H continuum; ii) the possible excess of photons able to ionise He^+ – with energy $h\nu > 54.4 \text{ eV}$ – emitted by the CSPN, compared to the black-body spectral energy distribution; iii) the differential dust absorption in the nebula.

Figure 19 illustrates the Zanstra discrepancy for Galactic PNe. Model predictions for $T_Z(H)$ and $T_Z(\text{He II})$ are derived from the conditions:

$$\mu_H Q(H^0) = 4\pi \int_{13.6}^{54.4} \frac{B_\nu[T_Z(H)]}{h\nu} d(h\nu) \quad (44)$$

$$\mu_{\text{He}^+} Q(\text{He}^+) = 4\pi \int_{54.4}^{\infty} \frac{B_\nu[T_Z(\text{He II})]}{h\nu} d(h\nu) \quad (45)$$

where B_ν is the Planck function and the other quantities have the usual meaning. It should be noted that we do not strictly follow the same procedure adopted by observers to obtain the Zanstra temperatures, which usually involves the ratio between nebular and stellar emission at particular wavelengths (the so-called Zanstra ratios; see e.g. Méndez et al. 1992). However, Eqs. (44) and (45) share the same basic assumptions, i.e. the nebula is considered in equilibrium state between ionisation and recombination

processes, and optically thick to the ionising continuum (ionisation-bounded).

The theoretical tracks in Fig. 19 account for the observed trend of the Zanstra discrepancy. From the analysis of the models it is worth reporting that i) at lower $T_Z(H)$ the Zanstra discrepancy increases with both the stellar mass and the transition time, and ii) the highest values of $T_Z(\text{He II})$ are attained by the most massive models; iii) there is some hint for an inverse Zanstra discrepancy (i.e. $T_Z(H) > T_Z(\text{He II})$) which may occasionally occur when the central star overcomes the hottest knee of its post-AGB track and starts to decline in luminosity.

Figure 20 contributes to investigate the causes of the Zanstra discrepancy. To this aim, we adopt the sample of 23 Galactic PNe analysed by Méndez et al. (1992), for which a large number of parameters are determined, including: the nebular masses and radii (see also Sect. 4.1), the masses of the CSPN, the effective temperatures, the Zanstra temperatures, etc. The observed data for $T_Z(H)$ and $T_Z(\text{He II})$ are plotted as a function of the quantity yL_a as defined by Méndez et al. (1992; see their table 4), which is equal to $\mu_H L$ according to their equation 12. The comparison with the theoretical predictions is then made for representative models whose stellar masses fall within the range indicated by Méndez et al.

The general accordance between the observed data and their expected location is remarkably good. The observed dispersion of the data in the $\log(\mu_H L) - \log T_Z(H)$ plane (see top-left panel of Fig. 20) is naturally accounted for by the models, which exhibit notable deviations from the horizontal parts (at constant luminosity) of the $\log L - \log T_{\text{eff}}$ post-AGB tracks. Such deviations show up as soon as the ionised shell becomes optically thin (i.e. $\mu_H < 1$) to the H continuum, which confirms the conclusions already drawn by Méndez et al. (1992). Note, however, that there is some offset in T_{eff} between observations and models, i.e. the latter get optically thin at lower effective temperatures than indicated by the data.

In the $\log(\mu_H L) - \log T_Z(\text{He II})$ plane (see top-right panel of Fig. 20) the models succeed in reproducing the corresponding data which, in this case, are expected to correspond to optically thick configurations to the He^+ continuum. It is also worth noticing that the agreement holds as well when the data are analysed as a function of the mass of the CSPN, as is clear by comparing the top panels (higher masses) to the bottom ones (lower masses) of Fig. 20. Finally, a general convergence is found with respect to the discrimination between optically thin/thick nebulae and their location in the observational planes.

4.5. Expansion velocities

The expansion velocities of PNe – usually derived from emission lines like H I, He II, [S II], [O II], [Ar IV], [Ne III], and more often [O III] – are found to range from few to $40 - 45 \text{ km s}^{-1}$, without any well-defined correlation with the nebular size (see Fig. 21).

Moreover, velocity estimates based on lines produced by ions with different ionisation potentials, have revealed the existence of velocity gradients across the nebulae (Gesicki et al. 1998). In general, the velocity is found to increase with the ionisation potential of the emitting ion, i.e. going from the inner to the outermost layers of the nebula. The fact that a large scatter (shown in Fig. 21) still characterises the velocity data, though derived from the same lines, likely points to a relatively broad range of parameters affecting the dynamics of PNe.

We attempt to investigate this point on the basis of the analytical prescriptions already presented in Sects. 2.4 and 2.7. We just recall that, although the adopted dynamical description is a simplified approach that cannot account for the complex velocity structure shown by hydrodynamical simulations (e.g. Schmidt-Voigt & Köppen 1987b; Marten & Schönberner 1991), nevertheless it should provide a reasonable representation of the average dynamical properties of the expanding nebulae. Furthermore, a clear improvement over similar analytical models is that the expansion of the nebula is not expressed with a single velocity, but the velocities of both the inner and outer rims of the ionised shell (V_S^* , and V_{ion} respectively) are predicted. In this way, the analytical model keeps track, to some extent, of the real velocity gradient inside the nebula.

An example is shown in Fig. 21 (top panel), where the two rim velocities are plotted as a function of R_{ion} . We can immediately notice the relatively large velocity range comprised by the two curves. In particular, quite low velocities (few km s^{-1}) are attained by the contact discontinuity during the early post-AGB stages, when the increased pressure due by ionisation slows down its expansion (see Sect. 2.7 for more discussion). Conversely, the ionisation front is always accelerating outward.

On the other hand, for purpose of easier comparison with observed data, we may also define an average expansion velocity

$$\langle V_{\text{exp}} \rangle = \frac{3}{4\pi(R_{\text{ion}}^3 - R_S^{*3})} \int_{R_S^*}^{R_{\text{ion}}} V(r) 4\pi r^2 dr \quad (46)$$

following Schmidt-Voigt & Köppen (1987b). In practice, it is a weighted mean over the nebular (emitting) volume, under the assumption that the velocity varies linearly between the two extrema V_S^* and V_{ion} . According to this definition $\langle V_{\text{exp}} \rangle$ is closer to V_{ion} , that is the maximum velocity.

The dependence of $\langle V_{\text{exp}} \rangle$ on the CSPN mass (for H-burning models) is evident already during the initial stages of the nebular expansion, so that the highest velocities are reached by the most massive models (see middle panel of Fig. 21). We can also notice that all the rising branches of the curves concentrate on a narrow range in radius, just reflecting the fact that the transition times of these models are comparable (i.e. 1500 yr in most cases). After the initial rise and peak, the curves start then to decline and finally flatten out at velocities of about $20 - 30 \text{ km}$

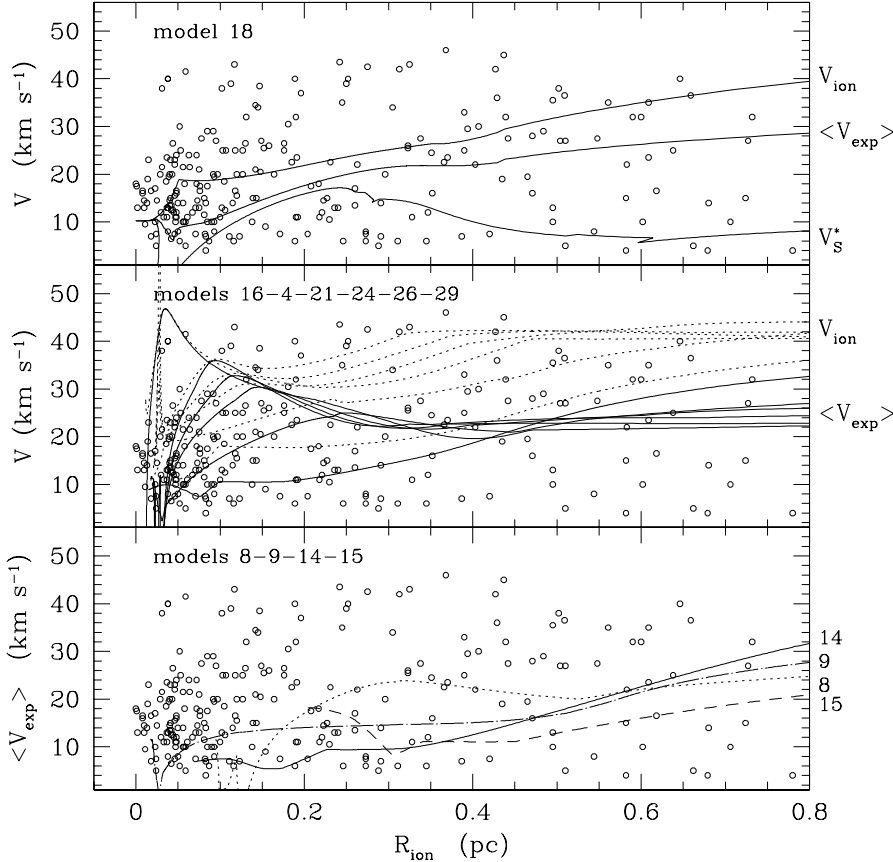


Fig. 21. Expansion velocities as a function of the nebular size of Galactic PNe. Data (circles) derived from the forbidden lines of [O III] and [O II] are taken from the compilation by Weinberger (1989). Model predictions are shown for comparison for several choices of the parameters. See text for further details

s^{-1} , which coincides with the mean range of the observed data. However, we remark again that this is a just a mean trend. For the same set of models the velocities of the outer rims are shown for comparison (dotted lines).

The initial radius of each velocity curve essentially represents the stage at which the nebula starts being ionised by the central star. This radius, $R_{\text{ion},0}$, can be expressed in first approximation as $V_{\text{AGB}}^{\text{max}} \times t_{\text{tr}}$, i.e. the product of the velocity of the ejected AGB material and the transition time. At increasing transition times, ionisation sets in at larger radii (compare model 4 with 8, having $t_{\text{tr}} = 1500$ and 8000 yr, respectively). The same effect is produced for lower values of the ejection velocity, as we can see in the bottom panel by comparing model 14 (solid line) with model 15 (short-dashed line), having both $t_{\text{tr}} = 10\,000$ yr, but $V_{\text{AGB}}^{\text{max}} \sim 6, 17 \text{ km s}^{-1}$ respectively. It follows that at least a part of the observed velocity spread of PNe at any radius can reflect differences in the evolutionary speed of the central star, as well as be the result of differences in the ejection velocity on the AGB.

It is worth also noticing the different behaviour of $\langle V_{\text{exp}} \rangle$ of PNe ionised by central stars that are either H- (e.g. model 4) or He-burners (e.g. model 9). On average, we expect that at given nebular size a PN ionised by a He-burning CS has a lower expansion velocity than that surrounding a H-burning CS of the same mass. This in turn would translate into longer dynamical ages, – de-

fined as $t_{\text{dyn}} = R_{\text{ion}}/V_{\text{exp}}$ – of PNe with He-burning CSs. This age difference offers a viable way to discriminate between the two classes of stars (see Dopita et al. 1996 for an application to PNe in the LMC).

On the basis of all mentioned points it is clear that, even if we are interested in average dynamical properties of PNe, the often adopted assumption of a constant expansion velocity can lead to substantial errors in the estimation of the true dynamical ages. Actually, it will be interesting to use our model results in a future analysis to address the discrepancy between the evolutionary and dynamical ages of PNe (see e.g. McCarthy et al. 1990).

4.6. Nebular line ratios

The ionisation structure and line emissivities are among the most basic properties of our PNe models, and can be easily checked by comparison with observations.

4.6.1. The He II/H β vs. [O III]/He II anticorrelation

Let us start with Figure 22, which combines the intensities of the three optical emission lines here considered, i.e. recombination (H β , He II $\lambda 4686$) and forbidden ([O III] $\lambda 5007$) lines.

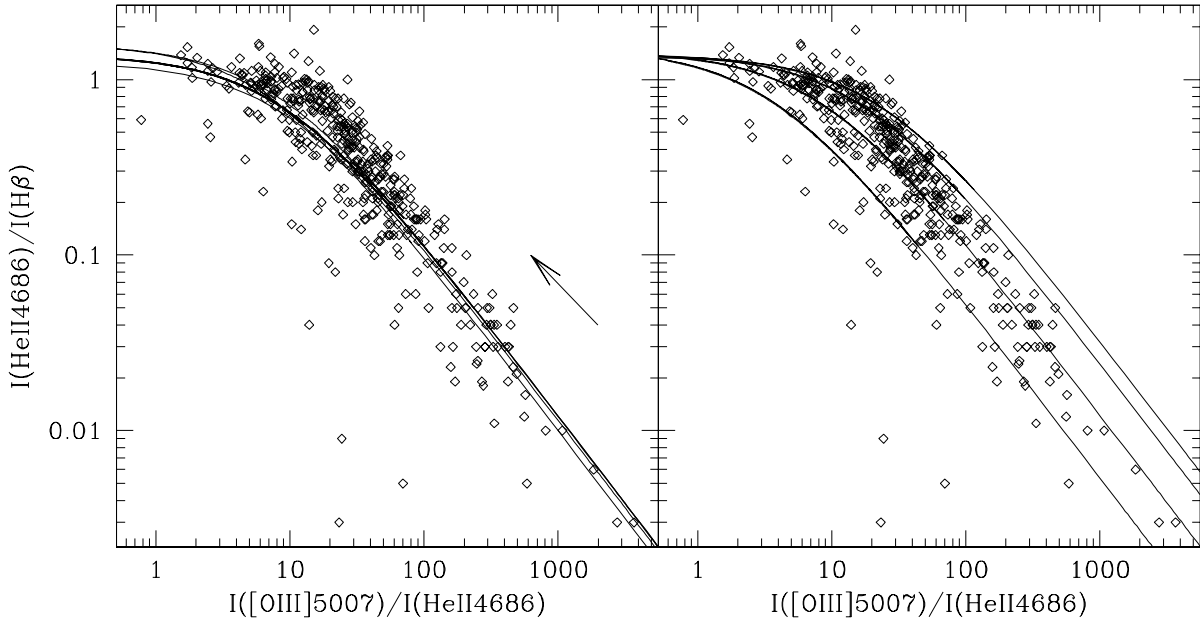


Fig. 22. Nebular line ratios in Galactic PNe. Data are taken from the Strasbourg-ESO Catalogue of Galactic Planetary Nebulae (Acker et al. 1992). Theoretical tracks are superimposed for comparison. Left panel: models 4–8–9–14–28, all calculated assuming a constant electron temperature $T_e = 10\,000$ K. Right panel: models 4–11–12–13, calculated with $T_e = 8\,000, 10\,000, 12\,000$ and $13\,000$ K (from higher to lower tracks). The arrow indicates the direction of increasing T_{eff}

First of all, we notice that the observed data do not present a large scatter, but rather follow a well-defined relation. There is an evident anticorrelation between the $\text{He II } \lambda 4686/\text{H}\beta$ and $[\text{O III}] \lambda 5007/\text{He II } \lambda 4686$ intensity line ratios, until the former becomes almost constant ($\gtrsim 1$) for low values of $[\text{O III}] \lambda 5007/\text{He II } \lambda 4686$.

The interpretation of such trend can be easily derived when considering that the ionisation potentials of He^+ (54.4 eV) and O^{++} (54.9 eV) are almost identical. It follows that the Strömgren volumes $V(\text{He}^+)$ and $V(\text{O}^{++})$ nearly coincides and the lines $\text{He II } \lambda 4686$ and $[\text{O III}] \lambda 5007$ are mainly produced within separate nebular regions, whose complementarity in emission volumes (i.e. when the innermost $V(\text{He}^{++})$ increases, the outer $V(\text{O}^{++})$ decreases and vice-versa) explains the observed anticorrelation between the respective line intensities.

It is also clear that since He^{++} is present in the nebula only if the central star is sufficiently hot, the observed trend in Fig. 22 implicitly contains a temperature scale (increasing along the direction of the arrow), and as a matter of fact, it has been used as a semi-empirical method to determine the temperature of high-excitation CSPN (see e.g. Gurzadyan 1988).

It is really striking how the empirical relation is so well reproduced by our models, which stands on few simple prescriptions for the ionisation and emission nebular structure (see Sect. 2.9). In this respect we draw the attention to the following points:

The flattening of the tracks towards the lowest $[\text{O III}] \lambda 5007/\text{He II } \lambda 4686$ values occurs when the nebulae

become optically-thin to both the H and He^+ continua. In fact, as the emission volumes for these ions are the same, the $\text{He II } \lambda 4686/\text{H}\beta$ intensity ratio depends only on atomic parameters (i.e. recombination coefficients and chemical abundances).

Finally, comparing the two panels of Fig. 22, it is evident that for given $\text{He II } \lambda 4686/\text{H}\beta$ intensity ratio, the relative intensity of the forbidden line is a strong function of the electron temperature (right-panel), whereas it is almost independent of other parameters (e.g. transition time, mass of the CSPN, H-/He-burning conditions, etc.). As expected, most of the observed data can be reproduced if T_e is varied from about 8 000 to 13 000 K, in agreement with the typical temperature range indicated by observations.

4.6.2. The evolution of the $I(\text{He II } \lambda 4686)/I(\text{H}\beta)$ line intensity ratio

Figure 23 shows the behaviour of the $I(\text{He II } \lambda 4686)/I(\text{H}\beta)$ intensity ratio as a function of the nebular radius. At smaller radii ($R_{\text{ion}} \lesssim 0.1$ pc), the observed data scatter over a large range, levelling up to values of 1. This trend is explained by the models as the result of the progressive increase of the stellar temperature at nearly constant luminosity, so that for $T_{\text{eff}} > 60\,000$ K helium starts to be doubly ionised and the recombination line $\text{He II } \lambda 4686$ starts to be detectable.

At this stage the nebula is already optically thin to the H-continuum (see Fig. 10). As the temperature in-

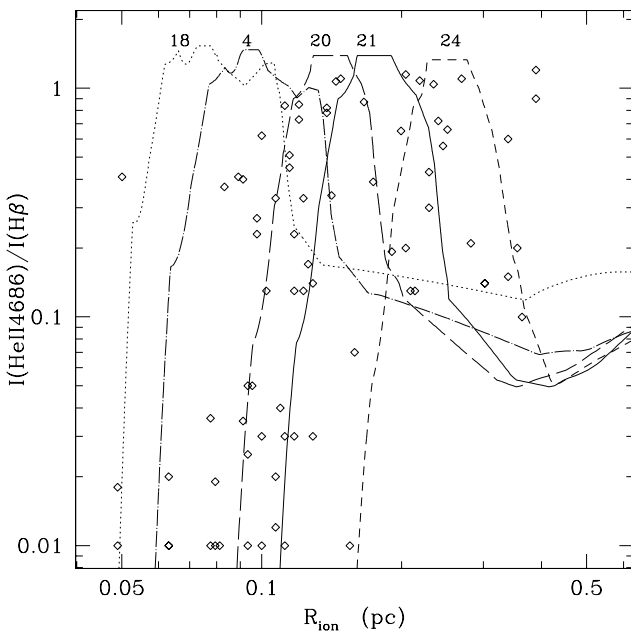


Fig. 23. Intensity line ratio as a function of the nebular size. Observed data refer to the sample of Galactic PNe analysed by Górný et al. (1997). Model predictions are shown for different choices of the CSPN mass

creases, the Strömgren volume $V(\text{He}^{++})$ grows (and the $\text{He II } \lambda 4686$ line intensity strengthens) until when it embraces the whole nebula, which then becomes optically thin also to the He-continuum. This occurs in correspondence to the maximum temperature attained close to the knee of the post-AGB track. As already mentioned, this condition yields the $I(\text{He II } \lambda 4686)/I(\text{H}\beta)$ line ratio to be practically constant and close to unity (as shown by the horizontal part of the tracks).

As soon as the stellar temperature starts declining, the Strömgren radius $R_{\text{ion}}(\text{He II})$ recedes inward, the $\text{He II } \lambda 4686$ intensity weakens the $\text{H}\beta$ line is still relatively strong (and the nebula still optically thin). We can notice that at some point in all models the decrease of the $I(\text{He II } \lambda 4686)/I(\text{H}\beta)$ line ratio slows down while the nebular radius is still increasing. This happens when the $\text{H}\beta$ line intensity is getting weaker as well and the nebula returns to be optically thick to the H-continuum. Such prediction is in perfect agreement with the observed lack of very low $I(\text{He II } \lambda 4686)/I(\text{H}\beta)$ line ratios at larger radii (i.e. $R_{\text{ion}} > 0.2$ pc).

5. Concluding remarks

In the present work we have presented in detail a new synthetic model for PN evolution. On the one hand, this model is kept simple by using convenient approximations for most physical processes, and by limiting their description to analytical relations that can easily be integrated with time. On the other hand, the model improves upon previous synthetic PNe models in the attempt i) to consistently couple the PN phase to the previous AGB evolution of the stellar precursor, and ii) to account for dynamical effects (like that produced by ionisation) that are believed important to the evolution of PNe.

Although the present description considers many aspects of the PN evolution, it cannot, of course, be considered exhaustive. Some approximations – like the assumptions spherical symmetry and constant electron temperature, and the somewhat simple description of the dynamical wind interactions – are in fact too crude if compared with the results of detailed hydrodynamical and photoionisation codes. However, this is the due price for fast computations. We remark that such synthetic codes probably provide the only way, at present times, to avoid the remarkable time requirements of hydrodynamical simulations.

This compromise is similar to that in the field of AGB evolution (see e.g. Groenewegen & Marigo 2001): AGB stars can be described either by i) complete stellar evolution codes, that due to their demand of CPU-time can be run only for few choices of stellar parameters, or by ii) synthetic AGB codes, that treat ill-known quantities by means of a parametric approach, and that can be easily run for any choice of parameters. Synthetic AGB models, although always recognised as crude tools, have had a crucial role in the understanding of many aspects of AGB evolution, and are widely considered to be fundamental in the field.

Similarly, our synthetic PNe code is fast enough to allow the systematic computation of extended grids of PNe tracks – for instance, for different choices of mass and metallicity distributions. The few free parameters (transition time, electron temperature, H-/He-burning tracks, etc.) can be constrained within reasonable limits by comparing the results with observations, in a way similar to the one we have presented in this paper. Anyway, none of these parameters is expected to be fixed for a given PNe population. In fact, the most promising way to explain the wealth of PNe characteristics, is that of performing Monte-Carlo simulations in which the free parameters are given reasonable probability distributions.

In the forthcoming papers, we will apply this approach to produce synthetic populations of PNe in different galaxies. Main targets will be:

- To further constrain the models by means of more detailed comparison with the observed properties of Galactic, Magellanic Cloud, and other PNe populations.
- To explore the expected distribution of chemical abundances among PNe, that may help to constrain synthetic TP-AGB models and their chemical yields.
- To simulate the PNe luminosity function in different galaxies, in order to test their suitability as extragalactic distance indicators.

Acknowledgements. We are grateful to K. Kifonidis and E. Müller for their constructive remarks on this work. P.M. thanks S.R. Pottasch and J.B. Salas for useful discussions

on PNe. An anonymous referee is acknowledged for interesting suggestions that could be fruitfully developed in future analyses. The work by L.G. has been partly financed by the Alexander von Humboldt-Stiftung, and the TMR grant ERBFMRXCT 960086. P.M. and L.G. also acknowledge the funding by the Italian MURST.

References

Acker A., Marcout J., Ochsenbein F., Stenholm B., Tylenda R., 1992, The Strasbourg-ESO Catalogue of Galactic Planetary Nebulae

Balick B., Gonzales G., Frank A., Jacoby G., 1992, *ApJ* 392, 582

Blöcker T., 1995, *A&A* 299, 755

Boffi F.R., Stanghellini L., 1994, *A&A* 284, 248

Breitschwerdt D., Kahn F.D., 1990, *MNRAS* 244, 521

Bressan A., Granato G.L., Silva L., 1998, *A&A* 332, 135

Ciardullo R., 1995, *Highlights of Astron.* 10, 507

Clegg R.E.S., Middlemass D., 1987, *MNRAS* 228, 759

Corradi R.M.L., Schönberner D., Steffen M., Perinotto M., 2000, *A&A* 354, 1071

de Freitas Pacheco J.A., Codina S.J., Viadana L., 1986, *MNRAS* 20,107

Dopita M.A., Vassiliadis E., Meatheringham S.J., et al., 1996, *AJ* 460, 320

Frank A., Balick B., Riley J., 1990, *AJ* 100, 1903

Frank A., van der Veen W.E.C.J., Balick B., 1994, *A&A* 282, 554

Gathier R., Pottasch S.R., 1989, *A&A* 209, 369

Gesicki K., Zijlstra A.A., Acker A., Szcerba R., 1998, *A&A* 329, 265

Gleizes F., Acker A., Stenholm B., 1989, *A&A* 222, 237

Górny S.K., Stasińska G., Tylenda R., 1997, *A&A* 318, 256

Groenewegen M.A.T., de Jong T., 1998, *A&A* 337, 797

Groenewegen M.A.T., Whitelock P.A., Smith C.H., Kerschbaum F., 1998, *MNRAS* 293, 18

Groenewegen M.A.T., Baas F., Blommaert J.A.D.L., Stehle R., Josselin E., Tilanus R.P.J., 1999, *A&AS* 140, 197

Groenewegen M.A.T., Marigo P., 2001, in AGB stars, Eds. H. Habing & H. Olofsson, Springer, in press

Gruenwald R., Viegas S.M., 2000, *ApJ* 543, 889

Gurzadjan G.A., 1988, *Ap&SS* 149, 343

Gussie G.T., Taylor A.R., 1994, *PASP* 106, 500

Habing H.J., Tignon J., Tielens A.G.G.M., 1994, *A&A* 286, 523

Ivezic Z., Elitzur M., 1995, *ApJ* 445, 415

Kafatos M., Lynch J.P., 1980, *ApJS* 42, 611

Kahn F.D., 1976, *A&A* 50, 145

Kahn F.D., 1983, in Planetary nebulae, IAU Symp. 103, 305

Kahn F.D., 1989, in Planetary Nebulae, IAU Symp. 131, 411

Kahn F.D., West K.A., 1985, *MNRAS* 212, 837

Kahn F.D., Breitschwerdt D., 1990, *MNRAS* 242, 505 (KB90)

Kifonidis K., 1996, Diploma Thesis, Technische Universität Berlin

Kurucz R.L., 1993, in The Stellar Populations of Galaxies, IAU Symp. 149, Eds. B. Barbuy and A. Renzini, Dordrecht: Kluwer, p. 225

Kurucz R.L., 1994, Kurucz CD-ROM No. 13, Smithsonian Astrophys. Obs.

Krüger D., Gauger A., Sedlmayr E., 1994, *A&A* 290, 573

Kwok S., 1983, in Planetary nebulae, IAU Symp. 103, 293

Kwok S., 1985, *ApJ* 290, 568

Kwok S., 2000, in The origin and evolution of planetary nebulae, Cambridge University Press (Cambridge astrophysics series 33)

Kwok S., Fitzgerald P.M., Purton C.R., 1978, *AJ* 219, L125

van Loon J.Th., Zijlstra A.A., Whitelock P.A., et al. 1998, *A&A* 329, 169

Loup C., Forveille T., Omont A., et al., 1993, *A&AS* 99, 291

Maciel W.J., Pottasch S.R., 1980, *A&A* 88, 1

Marigo P., 1998, *A&A* 340, 463

Marigo P., 2001, *A&A* 370, 194

Marigo P., Bressan A., Chiosi C., 1996, *A&A* 313, 545

Marigo P., Bressan A., Chiosi C., 1998, *A&A* 331, 564

Marigo P., Girardi L., Bressan A., 1999, *A&A* 344, 123

Marten H., Schönberner D., 1991, *A&A* 248, 590

McCarthy J.K., Mould J.R., Mendez R.H., et al., 1990, *ApJ* 351, 230

Mellema G., Frank A., 1995, *MNRAS* 273, 401

Méndez R.H., Kudritzki R.P., Herrero A., 1992, *A&A* 260, 329

Méndez R.H., Kudritzki R.P., Ciardullo R., Jacoby G.H., 1993, *A&A* 275, 543

Méndez R.H., Soffner T., 1997, *A&A* 312, 898

Netzer N., Elitzur M., 1993, *ApJ* 410, 701

Oliva E., Panagia N., 1983, *AP&SS* 94, 437

Osterbrock D.E., in *Astrophysics of gaseous nebulae*, 1974, University Science Books, Mill Valley, CA, p. 28

Pauldrach A., Puls J., Kudritzki R.P., 1988, *A&A* 207, 123

Peimbert M., 1990, *Rep. Prog. Phys.* 53, 1559

Péquignot D., Petitjean P., Boisson C., 1991, *A&A* 251, 680

Pottasch S.R., 1984, in *Planetary Nebulae. A Study of Late Stages of Stellar Evolution.*, Dordrecht: Reidel

Phillips J.P., 1998, *A&A* 340, 527

Renzini A., 1989, In *Planetary Nebulae*, IAU Symp. 131, Ed. S. Torres-Peimbert, Dordrecht: Kluwer, p. 391

Schmidt-Voigt M., Köppen J., 1987a, *A&A* 174, 211

Schmidt-Voigt M., Köppen J., 1987b, *A&A* 174, 223

Schönberner D., 1990, in *From Miras to planetary nebulae: which path for stellar evolution?*, Eds. M.O. Menessier & A. Omont, Editions Frontieres, Gif-sur-Yvette, France, p. 355

Schönberner D., Steffen M., 2000, in *Asymmetrycal Planetary Nebulae II: From Origins to Microstructures*, ASP Conf. Series 199, Eds. Kastener J.H., Soker N., Rappaport S., 59

Schwarz H.E., Corradi R.L.M., Melnick J., 1992, *A&AS* 96,23

Stanghellini L., Renzini A., 2000, *ApJ* 542, 308

Stasińska G., 1989, *A&A* 213, 274

Stasińska G., Tylenda R., 1986, *A&A* 155, 137

Stasińska G., Gorni S., Tylenda R., 1997, *A&A* 327, 736

Stasińska G., Richer M.G., McCall M.L., 1998, *A&A* 336, 667

Steffen M., Schönberner D., 2000, *A&A* 357, 180

Stoy R.H., 1933, *MNRAS* 93, 588

van Loon J.Th., 2000, *A&A* 354, 125

Vassiliadis E., Wood P.R., 1993, *ApJ* 413, 641 (VW93)

Vassiliadis E., Wood P.R., 1994, *ApJS* 92, 125

Volk K., Kwok S., 1985, *A&A* 153, 79 (VK85)

Wagenhuber J., Groenewegen M.A.T., 1998, *A&A* 340, 183

Weinberger R., 1989, *A&AS* 78, 301

Wood P.R., Whiteoak J.B., Hughes S.M.G., et al., 1992, *ApJ* 397, 552

Wood P.R., Alcock C., Allsman R.A., Alves D., Axelrod T.S., et al., 1999, *Asymptotic Giant Branch Stars*, IAU Symp. 191, Eds. T. Le Bertre, A. Lebre, and C. Waelkens, p. 151.

Zanstra H., 1931, *Publ. Dom. Astrophys. Obs. Victoria* 4, 209

Zhang C.Y., 1995, *ApJS* 98, 659

Zhang C.Y., Kwok S., 1998, *ApJS* 117, 341